







Cite this: *EES Catal.*, 2024,  
2, 157

## Gas-phase errors in computational electrocatalysis: a review

Ricardo Urrego-Ortiz, <sup>ab</sup> Santiago Builes, <sup>c</sup> Francesc Illas <sup>a</sup> and  
Federico Calle-Vallejo <sup>\*bd</sup>

Currently, computational models based on density functional theory (DFT) are intensively used for the analysis of electrocatalytic reactions and the design of enhanced catalysts. As the accuracy of these models is subjected to the quality of the input data, knowing the intrinsic limitations of DFT is crucial to improve computational predictions. A common pitfall of DFT is the estimation of the total energies of molecules, particularly those containing double and triple bonds. In this review, we show how gas-phase errors permeate thermodynamic and kinetic models of customary use in electrocatalysis, potentially compromising their predictiveness. First, we illustrate how these errors can be identified and provide a list of corrections for common molecules and functional groups. Subsequently, we explain how the errors spread from simple reaction energy calculations to adsorption energies, scaling relations, equilibrium potentials, overpotentials, and Sabatier-type activity plots. Finally, we list the remaining challenges toward an improved assessment of energetics at solid–gas–liquid interfaces.

Received 6th June 2023,  
Accepted 27th September 2023

DOI: 10.1039/d3ey00126a

[rsc.li/eescatalysis](http://rsc.li/eescatalysis)

### Broader context

The massive emissions of oxidized carbon and nitrogen species urgently call for an energetic transition that restores the balance to the biogeochemical cycles of those two elements. Electrochemical technologies such as electrolyzers are prominent alternatives to drive such a transition as they use electrical power from renewable sources to convert C- and N-containing pollutants into valuable feedstocks. However, electrochemical technologies currently rely on catalysts based upon scarce and expensive elements, which has motivated an intensive search for alternative materials preferably composed of earth-abundant elements. Computational models based on density functional theory (DFT) are extensively used for this purpose thanks to their reasonable tradeoff between accuracy and affordability. Nevertheless, DFT calculations usually entail large errors when predicting the energy of countless gaseous molecules commonly found as reactants and products of electrocatalytic reactions. In this review, we show how to detect and correct these errors in the gas phase, so as to prevent their spread over computational electrocatalysis models. The negative impact of these errors on the predictive power of electrocatalysis models is illustrated for a variety of reactions belonging to the carbon and nitrogen cycles.

## 1. Introduction

Contemporary computational electrochemistry has fostered a new era in the design of catalytic materials at the atomic scale.<sup>1–5</sup> Ever since the pioneering works of Nørskov, Rossmeisl

and coworkers, DFT-based electrochemical models have been extensively used to study and design efficient catalysts for key reactions in sustainable development, such as hydrogen evolution, oxygen reduction and evolution, and the production of fuels and commodity chemicals from CO<sub>2</sub>.<sup>5–11</sup> Nowadays, computational electrochemistry is a prominent tool to address the colossal challenges of climate change and the much-needed energy transition.<sup>4</sup>

The reliability of DFT-based computational models depends on the method employed to approximate the exact but unknown universal exchange–correlation functional (xc-functional). This poses an often unnoticed but important constraint in heterogeneous (electro)catalysis where gas–liquid–solid interfaces ought to be suitably described, which is hardly achieved by a single functional chosen among the existing families.<sup>12,13</sup> For instance, hybrid functionals are widely used to accurately predict

<sup>a</sup> *Departament de Ciència de Materials i Química Física & Institut de Química Teòrica i Computacional (IQTCUB), Universitat de Barcelona, C/ Martí i Franquès 1, 08028 Barcelona, Spain*

<sup>b</sup> *Nano-Bio Spectroscopy Group and European Theoretical Spectroscopy Facility (ETSF), Department of Polymers and Advanced Materials: Physics, Chemistry and Technology, University of the Basque Country UPV/EHU, Av. Tolosa 72, 20018 San Sebastián, Spain. E-mail: federico.calle@ehu.es*

<sup>c</sup> *Escuela de Ciencias Aplicadas e Ingeniería, Universidad EAFIT, Carrera 49 # 7 sur 50, 050022, Medellín, Colombia*

<sup>d</sup> *IKERBASQUE, Basque Foundation for Science, Plaza de Euskadi 5, 48009 Bilbao, Spain*



molecular properties but fail in the description of metals,<sup>14–16</sup> whereas affordable functionals at the generalized gradient approximation (GGA) provide fair results for conductive solids and surfaces but possess serious limitations for gases, such as the well-known overbinding of O<sub>2</sub> and N<sub>2</sub>.<sup>17–19</sup> Meta-GGA functionals supposedly improve the deficiencies of GGAs for molecules while maintaining the accuracy for solids and surfaces, but their use in (electro)catalysis is still incipient due to their high computational cost, convergence problems, and because they have not been shown yet to outperform GGA functionals in terms of chemisorption.<sup>18,20,21</sup>

Although gas-phase errors in GGA functionals have been exposed using datasets containing mainly small molecules,<sup>22–24</sup> recent works show that such errors also permeate meta-GGA and hybrid functionals for the prediction of thermodynamic properties of molecules with environmental and industrial

relevance, such as nitrates, carboxylic acids and several other families of organic compounds, and hydrogen peroxide.<sup>25–29</sup> This implies that accurate estimations of basic properties and parameters in electrocatalysis, such as adsorption/desorption energies and equilibrium potentials, are not guaranteed by simply climbing the so-called Jacob's ladder of accuracy.<sup>30</sup> In fact, accurate predictions may rely on error cancellation more often than we think, which occurs when the DFT errors of the reactants and products are similar.<sup>31–33</sup> This condition is not always met, as attested by the CO<sub>2</sub> reduction to CO and numerous reactions among nitrogen oxides,<sup>25,34</sup> so it is advisable to assess the gas-phase errors of each compound separately.

Because DFT-based models have become customary in (electro)catalysis and most often use GGA functionals, it is crucial to assess the impact of gas-phase errors on their predictiveness. In this review, we first summarize various methods for identifying



**Ricardo Urrego-Ortiz**

*Ricardo Urrego-Ortiz received his BSc degree in Process Engineering from EAFIT University (Colombia) in 2017. Later, he worked as a project engineer and data scientist in a company focused on energy efficiency. In 2021, Ricardo obtained his MSc in engineering at EAFIT University. Currently, he is a PhD student at the University of Barcelona funded by "la Caixa" Foundation. Ricardo uses theoretical chemistry and computational tools to address major societal and environmental challenges, such as the imbalance of the nitrogen and carbon cycles, and the transition from fossil fuels toward sustainable energy sources.*



**Santiago Builes**

*Santiago Builes is a professor of process engineering at EAFIT University (Colombia). He received his PhD degree (2012) in materials science from the Autonomous University of Barcelona (Spain). Afterwards, he was a postdoctoral researcher at the University of Delaware (USA). Santiago applies molecular modeling and computational chemistry to address environmental challenges and obtain a better understanding of industrial processes. His research focuses on atomistic simulations of separation processes and (electro)catalysis, in areas such as carbon capture and utilization.*



**Francesc Illas**

*Francesc Illas is a Full Professor of Physical Chemistry at the University of Barcelona. He spent several periods at IBM Almaden Research Center and Los Alamos National Laboratory and was invited professor at Università della Calabria (Italy) and Université Pierre et Marie Curie (France). He has received several awards, was elected Fellow of the European Academy of Sciences (2009), of the Academia Europaea (2017) and is the recipient of the 2022 Medal of the Spanish Royal Society of Chemistry. His research involves the application of theoretical and computational chemistry methods to surface chemistry and heterogeneous catalysis.*



**Federico Calle-Vallejo**

*After his degree in chemical engineering in Colombia, Federico Calle-Vallejo did his PhD at DTU (Denmark) and was a postdoctoral researcher at Leiden University (the Netherlands) and ENS Lyon (France). Subsequently, he was a Veni research fellow at Leiden University and a Ramón y Cajal research fellow at the University of Barcelona (Spain). Currently, Federico Calle-Vallejo is an Ikerbasque Research Associate and Visiting Professor at the University of the Basque Country (Spain). Federico's group uses DFT and in-house methods and descriptors to make predictive models of electrocatalytic reactions with structural and compositional sensitivity.*



and quantifying these errors. Next, we explain how they affect calculated properties ranging from simple equilibrium potentials and adsorption energies to more complex Sabatier-type analyses based on scaling relations and volcano plots. Finally, we provide a brief overview of the challenges lying on the way toward an accurate DFT modeling of electrocatalytic reactions involving molecules at surfaces.

## 2. Detection and quantification of DFT gas-phase errors

### 2.1 Basic error formulations

For a reaction in the gas phase, the enthalpy ( $\Delta_r H_{\text{DFT}}$ ) and Gibbs energy ( $\Delta_r G_{\text{DFT}}$ ) change can be estimated from DFT calculations using the following equations:

$$\Delta_r H_{\text{DFT}} \approx \Delta E_{\text{DFT}} + \Delta \text{ZPE} + \int \Delta C_p dT \quad (1)$$

$$\Delta_r G_{\text{DFT}} = \Delta_r H_{\text{DFT}} - T\Delta S \quad (2)$$

In eqn (1),  $\Delta E_{\text{DFT}}$  is the sum of the DFT energies of the products multiplied by their respective stoichiometric coefficients minus the DFT energies of the reactants also multiplied by their respective stoichiometric coefficients. Analogously,  $\Delta \text{ZPE}$  is the change in the zero-point energies of products and reactants calculated through the harmonic oscillator approximation, and  $\int \Delta C_p dT$  is the change in the heat capacity contribution, which is usually neglected because of the cancellation of the contributions of products and reactants in the range of 0 to 298.15 K.<sup>6,28,35</sup> However, we anticipate that this term may not be negligible for reactions with numerous proton–electron transfers. In eqn (2),  $T\Delta S$  represents the difference between the total entropies of the products and reactants, usually taken from thermodynamic tables.<sup>1,36</sup>

Eqn (1) and (2) can be compared to the corresponding experimental values ( $\Delta_r H_{\text{exp}}$  and  $\Delta_r G_{\text{exp}}$ , respectively), thus allowing to define a total DFT error ( $\varepsilon_{\text{T}}$ ) as per eqn (3).<sup>25,34</sup>

$$\varepsilon_{\text{T}} = \Delta_r G_{\text{DFT}} - \Delta_r G_{\text{exp}} = \Delta_r H_{\text{DFT}} - \Delta_r H_{\text{exp}} \quad (3)$$

Note in passing that the equality in eqn (3) only holds when experimental  $T\Delta S$  values are used in addition to the DFT calculations, which is most often the case.<sup>1,6,25,37,38</sup> Furthermore, the total error  $\varepsilon_{\text{T}}$  results from the errors of the products ( $\varepsilon_{\text{P}}$ ) and the reactants ( $\varepsilon_{\text{R}}$ ), as shown in eqn (4).<sup>25,34</sup> Importantly, in eqn (4) the individual errors in  $\varepsilon_{\text{P}}$  and  $\varepsilon_{\text{R}}$  are multiplied by their respective stoichiometric coefficients.

$$\varepsilon_{\text{T}} = \sum \varepsilon_{\text{P}} - \sum \varepsilon_{\text{R}} \quad (4)$$

When adsorption reactions are analyzed, the errors in the catalyst ought to be considered. Because adsorbed species are not free but part of the solid phase, their errors are expected to be different from those of their molecular counterparts. So far, only a few works can be found in the literature devoted to pinpointing and estimating errors in adsorbates.<sup>39–41</sup> Here we

focus on gas-phase errors and encourage the future analysis of errors in the solid state.

Finally, we note that convergence tests are usually carried out to rule out that gas-phase errors come from an inadequate selection of the setup of the DFT calculations. For plane-wave codes, this is ensured by showing that the variations in the Gibbs energy of a prototypical reaction are within 0.05 eV as a function of the plane-wave energy cutoff.<sup>25,27,28,34,42</sup>

### 2.2 Pinpointing individual errors

Numerous studies have exposed significant DFT errors for several molecules in the gas phase using different xc-functionals,<sup>23,43–49</sup> and  $\Delta E_{\text{DFT}}$  has been identified as the main error source since the ZPEs are generally in line with experiments,<sup>29</sup> simply because the harmonic calculated vibrational frequencies are generally rather accurate. As reasonable predictions of gas-phase energetics should not rely on error cancellation, namely when  $\sum \varepsilon_{\text{P}} \approx \sum \varepsilon_{\text{R}}$  in eqn (4), significant efforts have recently been devoted to pinpoint and estimate the errors in  $\Delta E_{\text{DFT}}$  of gaseous compounds in a systematic manner. The most common methods are the following:

**(i) Experiment-based statistical fitting.** This approach was used in the pivotal study of Peterson *et al.*,<sup>6</sup> where DFT was used to detail the electrocatalytic reduction mechanism toward  $\text{C}_1$  species from  $\text{CO}_2$ .

To identify if a molecule or certain chemical structure is a potential source of error, the authors collected several reactions involving that molecule/structure and available experimental reaction enthalpy data. Then, the DFT-calculated energies of those reactions were compared to the experimental ones and the mean absolute error (MAE) calculated. A statistical analysis was performed by artificially varying the DFT-calculated energy ( $E_{\text{DFT}}$ ) of the “problematic” molecule until the MAE was minimized. The difference between the value that minimizes the MAE and the calculated DFT energy of the molecule is taken as its error. Statistical analyses can be performed simultaneously for multiple compounds or structures provided that the set of chemical reactions is sufficiently large and experimental data are available.

Using this approach, the authors found large PBE errors for CO (−0.51 eV) and large RPBE errors for  $\text{CO}_2$  (0.45 eV) and proposed the OCO backbone as a problematic group of atoms that affects numerous compounds in the carbon cycle for RPBE, including carboxylic acids and esters. In Fig. 1a, the sensitivity analysis used to obtain the RPBE error of the OCO backbone is presented: the MAE is minimized when an error of 0.45 eV is assigned to the compounds including an OCO backbone in their structure. The MAE of bystander reactions, that is the reactions that do not involve OCO-containing species, remains constant upon applying the corrections.

Along these lines, other studies have used experimental formation enthalpies and free energies to show that functional groups, as defined in organic chemistry, introduce systematic, additive errors.<sup>25,34</sup> Fig. 1b shows how the PBE error of the carbonyl group (−C=O−) is obtained using a set of 5 molecules with known experimental formation energies after accounting





**Fig. 1** Summary of the statistical methods that use experiments as a reference to identify and quantify the errors in the DFT energy of gas-phase compounds. (a) The black line shows the MAE minimization through sensitivity analysis of the OCO backbone error for RPBE for reactions involving CO<sub>2</sub>, HCOOH, CH<sub>3</sub>COOH and HCOOCH<sub>3</sub>. In red, the unaffected MAE of reactions not involving OCO-containing molecules. Reproduced from ref. 6 Copyright 2010, Royal Society of Chemistry. (b) Determination of the carbonyl group (–C=O–) error in PBE from a dataset of 5 molecules, considering that alkane groups (CH<sub>x</sub>) also contribute to the total error. Reproduced from ref. 34, licensed under CC-BY-NC-ND (<https://creativecommons.org/licenses/by-nc-nd/4.0/>). (c) Functional groups with appreciable DFT errors in organic compounds. Adapted from ref. 25 Copyright 2021, John Wiley and Sons.

for the respective linear alkane group error (–CH<sub>x</sub>),<sup>34</sup> and Fig. 1c shows various C- and N-containing functional groups. The errors in those groups were estimated for four GGA functionals in a similar manner and are compiled in Table 1.

**(ii) Statistical fitting based on xc-functional ensembles.** Christensen *et al.* proposed to identify problematic molecules and/or chemical structures by studying the systematic correlations between DFT predictions instead of calculating errors with respect to experiments.<sup>40</sup> In this case, a set of reactions is also used. In fact, the same reaction set used by Peterson *et al.*<sup>6</sup> was used as a case study by Christensen *et al.*<sup>40</sup>

In this correction scheme, the DFT energies of two reactions obtained with different xc-functionals are compared. If a linear correlation is obtained, it is considered that at least one error source is present for all xc-functionals, namely an ill-represented

molecule/chemical structure. The slope of such linear relation is rationalized as the change in the number of occurrences of the problematic molecule/structure in the y-axis reaction *versus* the change in the x-axis reaction. For example, Fig. 2 correlates the reaction enthalpies of H<sub>2</sub> + CO<sub>2</sub> → HCOOH (reaction (2)) and 3H<sub>2</sub> + CO<sub>2</sub> → CH<sub>3</sub>OH + H<sub>2</sub>O (reaction (3)) obtained with several xc-functionals. The authors used GGA functionals accounting or not for van der Waals (vdW) interactions, such as BEEF-vdW and PBE, and 2000 functionals obtained by varying the expansion coefficients of BEEF-vdW.<sup>52</sup> Advantageously, this approach allows to predict errors in adsorbed species without using experimental heats of adsorption, which are scarce in the literature.<sup>21</sup>

If the OCO backbone is assumed to be the main error source in the reactions of Fig. 2, a linear correlation with a slope of 0 is expected since the OCO backbone in the first reaction is





**Table 1** DFT errors of molecules and functional groups containing C, N, O, and H, see also Fig. 1c

Molecule or functional group	PBE	PW91	RPBE	BEEF-vdW
O <sub>2</sub> <sup>a</sup>	-0.46	-0.33	-0.74	-0.81
N <sub>2</sub>	0.34	0.38	-0.05	-0.32
CO <sub>2</sub> <sup>b</sup>	-0.19	-0.15	-0.46	-0.56
CO <sup>b</sup>	0.24	0.25	-0.07	-0.18
H <sub>2</sub> O <sub>2</sub> <sup>c</sup>	-0.26	-0.23	-0.29	-0.34
NO <sup>d</sup>	-0.07	0.05	-0.41	-0.58
NO <sub>2</sub> <sup>d</sup>	-0.80	-0.66	-1.12	-1.27
NO <sub>3</sub> <sup>d</sup>	-1.41	-1.26	-1.72	-1.92
N <sub>2</sub> O <sup>d</sup>	-0.50	-0.41	-0.86	-1.10
HNO <sup>d</sup>	-0.05	-0.01	-0.30	-0.43
HNO <sub>2</sub> <sup>d</sup>	-0.54	-0.48	-0.78	-0.95
HNO <sub>3</sub> <sup>d</sup>	-0.96	-0.87	-1.14	-1.35
NO <sub>2</sub> (aq) <sup>-de</sup>	-0.54	-0.48	-0.78	-0.95
NO <sub>3</sub> (aq) <sup>-de</sup>	-0.96	-0.87	-1.14	-1.35
cis-N <sub>2</sub> O <sub>2</sub> <sup>d</sup>	-0.71	-0.55	-1.25	-1.59
N <sub>2</sub> O <sub>3</sub> <sup>d</sup>	-1.19	-1.06	-1.66	-2.04
N <sub>2</sub> O <sub>4</sub> <sup>d</sup>	-1.80	-1.63	-2.22	-2.62
N <sub>2</sub> O <sub>5</sub> <sup>d</sup>	-2.04	-1.86	-2.42	-2.87
Amine, -NH <sub>x</sub>	0.00	0.00	0.04	-0.09
Nitro, -NO <sub>2</sub>	-0.65	-0.57	-0.81	-1.08
Nitrate, -NO <sub>3</sub>	-1.00	-0.91	-1.17	-1.45
Nitrite, -ONO	-0.56	-0.50	-0.79	-1.02
Hydroxylamine, -(NH <sub>x</sub> OH <sub>y</sub> )	-0.16	-0.15	-0.15	-0.31
Phenyl, -Ph	-0.06	-0.12	-0.13	0.17
Aniline, -(N-Ph)-	-0.16	-0.21	-0.16	0.05
Hydrazine, -(N-N)-	-0.09	-0.08	-0.05	-0.21
Amide, -(C=O)NH <sub>2</sub>	-0.17	-0.15	-0.20	-0.38
Nitrile, -CN	0.10	0.11	-0.17	-0.33
n-Alkane*, -CH <sub>x</sub>	0.036	0.015	0.086	0.203
Iso-carbon alkane, -CH-	0.13	0.12	0.25	0.20
Neo-carbon alkane, -C-	0.22	0.21	0.38	0.27
Carbonyl, -C=O <sup>-a</sup>	-0.10	-0.10	-0.21	-0.27
Carboxyl, -(C=O)O <sup>-a</sup>	-0.19	-0.19	-0.27	-0.34
Hydroxyl, -OH <sup>a</sup>	-0.04	-0.04	-0.01	-0.14

<sup>a</sup> Errors obtained from ref. 26. Unmarked errors are taken from ref. 25.<sup>b</sup> Errors obtained from ref. 34. <sup>c</sup> Errors obtained from ref. 27. <sup>d</sup> Errors obtained from ref. 29. <sup>e</sup> The errors of NO<sub>3</sub>(aq)<sup>-</sup> and NO<sub>2</sub>(aq)<sup>-</sup> correspond to those of HNO<sub>3</sub>(g) and HNO<sub>2</sub>(g), respectively.<sup>50,51</sup>

preserved (it is present both in CO<sub>2</sub> and HCOOH) while in the second reaction it is consumed, thus 0/−1 = 0. However, if the C=O error is assumed to be dominant, the observed slope of 0.5 is obtained as only one of the two C=O in CO<sub>2</sub> is consumed in the first reaction (HCOOH preserves one C=O), while the two C=O are consumed in the second reaction, hence −1/−2 = 0.5. After identifying the C=O bond as the main source of error, its individual correction could be obtained by comparison to experimental data following the approach described before in (i). Note in passing that the errors associated to adsorbed species can also be calculated for a given adsorbate and material by means of adsorption-energy scaling relations, as explained in detail in Section 5.<sup>39</sup>

**(iii) Deterministic error isolation using formation energies.**

Unlike the previous two approaches, this one is not statistical and only requires the experimental formation energy of a gaseous compound to determine its DFT error.<sup>25,29</sup> The formation reaction of a generic gaseous compound H<sub>x</sub>N<sub>β</sub>C<sub>γ</sub>O<sub>δ</sub> from its elements in their standard states can be written as follows:

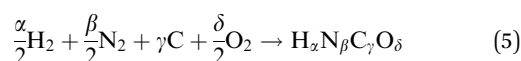


**Fig. 2** Correlations between the enthalpies of reactions 2 (H<sub>2</sub> + CO<sub>2</sub> → HCOOH) and 3 (3H<sub>2</sub> + CO<sub>2</sub> → CH<sub>3</sub>OH + H<sub>2</sub>O) calculated with ensembles of xc-functionals. Each color represents the result for a functional: PBE in blue, RPBE in red, vdW-DF in green, vdW-DF2 in orange, BEEF-vdW in black and outlined in red, and the ensemble of functionals obtained from BEEF-vdW are in gray. The red cross corresponds to the experimental value. Reproduced with permission from ref. 40, licensed under CC-BY 3.0 (<https://creativecommons.org/licenses/by/3.0/>)/Cropped from original.

From eqn (3), the total DFT error of the formation reaction of the compound H<sub>x</sub>N<sub>β</sub>C<sub>γ</sub>O<sub>δ</sub> can be expressed as:

$$\begin{aligned} \varepsilon_T &= \Delta_f G_{\text{H}_x\text{N}_\beta\text{C}_\gamma\text{O}_\delta}^{\text{DFT}} - \Delta_f G_{\text{H}_x\text{N}_\beta\text{C}_\gamma\text{O}_\delta}^{\text{exp}} \\ &= \Delta_f H_{\text{H}_x\text{N}_\beta\text{C}_\gamma\text{O}_\delta}^{\text{DFT}} - \Delta_f H_{\text{H}_x\text{N}_\beta\text{C}_\gamma\text{O}_\delta}^{\text{exp}} \end{aligned} \quad (6)$$

The use of enthalpies ( $\Delta_f H_{\text{H}_x\text{N}_\beta\text{C}_\gamma\text{O}_\delta}^{\text{exp}}$ ) or Gibbs energies ( $\Delta_f G_{\text{H}_x\text{N}_\beta\text{C}_\gamma\text{O}_\delta}^{\text{exp}}$ ) is facultative and usually depends on the availability of experimental data. In principle, the errors calculated from free energies and enthalpies should be identical. However, it is probably more advisable to make the error assessment on the basis of Gibbs energies, as they are connected to the equilibrium potentials of electrochemical reactions, see Section 3. Moreover, by means of eqn (4), the total error can be further decomposed into the difference between the errors of the reactants (H<sub>2</sub>, N<sub>2</sub>, C, and O<sub>2</sub>) and products (H<sub>x</sub>N<sub>β</sub>C<sub>γ</sub>O<sub>δ</sub>) considering their stoichiometric coefficients given in eqn (5).

$$\varepsilon_T = \varepsilon_{\text{H}_x\text{N}_\beta\text{C}_\gamma\text{O}_\delta} - \left( \frac{\alpha}{2}\varepsilon_{\text{H}_2} + \frac{\beta}{2}\varepsilon_{\text{N}_2} + \gamma\varepsilon_{\text{C}} + \frac{\delta}{2}\varepsilon_{\text{O}_2} \right) \quad (7)$$

If eqn (6) and (7) are combined, the DFT error of the gaseous compound H<sub>x</sub>N<sub>β</sub>C<sub>γ</sub>O<sub>δ</sub> can be isolated:

$$\begin{aligned} \varepsilon_{\text{H}_x\text{N}_\beta\text{C}_\gamma\text{O}_\delta} &= \left( \Delta_f G_{\text{H}_x\text{N}_\beta\text{C}_\gamma\text{O}_\delta}^{\text{DFT}} + \frac{\alpha}{2}\varepsilon_{\text{H}_2} + \frac{\beta}{2}\varepsilon_{\text{N}_2} + \gamma\varepsilon_{\text{C}} + \frac{\delta}{2}\varepsilon_{\text{O}_2} \right) \\ &\quad - \Delta_f G_{\text{H}_x\text{N}_\beta\text{C}_\gamma\text{O}_\delta}^{\text{exp}} \end{aligned} \quad (8)$$

Eqn (8) can be simplified by noting that DFT usually yields good predictions for hydrogen<sup>49</sup> and graphene, which is often employed as the reference to model carbon instead of graphite due to the weak interlayer forces of the latter.<sup>53–58</sup> Hence,  $\varepsilon_{\text{H}_2} \approx \varepsilon_{\text{C}} \approx 0$ . Furthermore,  $\varepsilon_{\text{O}_2}$  can be explicitly calculated from the water formation reaction (WFR: H<sub>2</sub> +  $\frac{1}{2}$ O<sub>2</sub> → H<sub>2</sub>O) assuming





Fig. 3 Errors of several nitrogen oxides as a function of the number of oxygen atoms in their structure for various xc-functionals: (a) PBE, (b) PW91, (c) RPBE, and (d) BEEF-vdW. In all panels, blue, red, and green are the trends of molecules with the general formulas  $N_2O_x$ ,  $NO_x$ , and  $HNO_x$ , respectively. The linear equation is reported in each case. Reproduced from ref. 29, licensed under CC BY 4.0 (<https://creativecommons.org/licenses/by/4.0/>).

that the error in the calculated energy of  $H_2O$  is negligible,<sup>31</sup> and  $\epsilon_{N_2}$  from the ammonia synthesis reaction<sup>25</sup>  $\left(ASR: \frac{1}{2}N_2 + \frac{3}{2}H_2 \rightarrow NH_3\right)$ , as  $NH_3$  is also reasonably well described by DFT.<sup>49</sup> From the WFR we obtain eqn (9), and the ASR yields eqn (10).

$$\epsilon_{O_2} = -2(\Delta_f G_{WFR}^{DFT} - \Delta_f G_{WFR}^{exp}) \quad (9)$$

$$\epsilon_{N_2} = -2(\Delta_f G_{ASR}^{DFT} - \Delta_f G_{ASR}^{exp}) \quad (10)$$

In Fig. 3, the DFT errors of different nitrogen oxides ( $N_2O_x$ ,  $HNO_x$ , and  $NO_x$ ) calculated using eqn (8)–(10) for four xc-functionals are shown as a function of the number of oxygen atoms in the molecules.

**(iv) Chemically intuitive and automated approaches.** Recent work<sup>28</sup> proposed a chemically intuitive sequence to decompose the DFT error of a molecule into contributions from specific groups of atoms and/or bonds. To deconvolute the errors, a set of molecules sharing structural similarities is necessary. Consequently, as a case study, the authors analyzed thirteen compounds containing nitrogen, oxygen, and hydrogen. The full dataset can be corrected in three different ways, as summarized below.

First, one can assume that the DFT errors of groups of atoms are equal to those encountered in analogous molecules, and then sequentially correct the errors of larger compounds (e.g., the molecule  $NO_2$  is analogous to the  $ONO$  backbone in  $HNO_2$  and  $HNO_3$  and, thus, their errors are assumed to be identical).

In principle, the sequence progresses from simple (small) to complex (large) molecules. The flowchart of this procedure, referred to as “sequential”, is provided in Fig. 4, where each gray step deals with a specific group of atoms.

Second, as shown in Table 2,<sup>28</sup> a matrix representation of each molecule can serve as the basis to identify ill-described bonds within the molecules of the dataset. Once the structure of each molecule in the dataset is represented by the (single, double, triple) bonds between the atoms, an automatic optimization can be made using as free parameters the errors in the bonds. Along the lines of previous approaches,<sup>6,40</sup> the MAE and MAX (or combinations thereof) with respect to experimental formation energies can be used as objective functions and minimized. In principle, this requires less human input than the method based on chemical intuition but leads to larger residual errors upon optimization. This procedure is referred to as automatic optimization 1 (AO1). For instance,  $HNO_{3(g)}$  contains two N–O bonds and one N=O bond, as shown in Fig. 5a.

Third, the errors of the groups of atoms identified by means of the sequential approach are set as adjustable parameters in an optimization problem, see Table 2. Since there are several possibilities to represent the molecules, multiple representations may lead to different correction schemes with varying performance. In such cases, it is advisable to make an ensemble of representations and choose the one providing lower final errors. We refer to this procedure as automatic optimization 2 (AO2). Fig. 5b depicts how  $HNO_{3(g)}$  can be decomposed into  $ONO$  and  $NOH$  groups.

Fig. 6 summarizes the performance of the (i) sequential, (ii) AO1, and (iii) AO2 approaches when used to correct the PBE-calculated Gibbs energies of the thirteen nitrogen compounds listed in Table 2. The MAE and MAX values before and after the corrections are shown for each method. Table 3 shows the problematic groups of atoms and/or bonds identified by each method with their respective errors. All the methods substantially decrease the large, uncorrected MAE (0.83 eV) and MAX (1.98 eV) obtained with plain PBE. Moreover, the three methods use the same number of variables: both AO2 and the sequential approach identified five problematic structures, and AO1 employs five different bonds to correct the errors in the Gibbs energies. AO2 yields the lowest errors (final MAE/MAX of 0.05/0.08 eV), followed by the sequential method, which resulted in a similar MAE of 0.07 eV but a larger MAX of 0.19 eV. Finally, AO1 produces the largest residual errors, with a MAE of 0.11 eV and a MAX of 0.26 eV.

### 2.3 Anticipating error cancellation

Once estimated, the DFT errors of the molecules can be used to anticipate the degree of error cancellation in a chemical reaction. Granda-Marulanda *et al.*<sup>34</sup> assessed the errors of  $CO_2$  and  $CO$  and noted a constant difference between them of  $\sim 0.40$  eV for various GGA functionals, see Fig. 7. Hence, DFT at the GGA level is unable to simultaneously provide an accurate description of both molecules and one cannot rely on error cancellation for several important catalytic reactions, such as  $CO_2$  electroreduction to  $CO$  and  $CO$  electrooxidation to  $CO_2$ , and the water–gas





Fig. 4 Flowchart of the chemically intuitive sequential method to detect the gas-phase errors of increasingly large molecules with N, O and H. Blue parallelograms represent the different sets of molecules and gray boxes represent the evaluation of specific errors in their thermochemical data. Reproduced from ref. 28, licensed under CC BY 4.0 (<https://creativecommons.org/licenses/by/4.0/>).

shift and its reverse reaction in heterogeneous catalysis. Similarly, it has been shown that the error difference between the nitro and nitrite functional groups is also constant and no larger than  $\sim 0.10$  eV for different GGAs.<sup>25</sup> In view of such moderate errors, for reactions between similar species or functional groups, such as the nitro-nitrite isomerization, error cancellation can be expected.

Before closing this section, we note that the aforementioned methods are based on different considerations and thus yield different types and number of errors, with varying numerical results. Depending on data availability and the nature of the intended calculations, one could be preferred over the others. However, as each approach is formulated differently, it is advisable to consistently use the same approach throughout a given study. Regardless of the scheme chosen, a detailed appraisal of gas-phase errors is advised at the early stages of any DFT-based electrocatalysis study for the reasons explained in the next sections. Furthermore, we emphasize that the values in Table 1 can be used to model any electrocatalytic reaction involving the species and functional groups therein, as long as the compounds are in the gas phase. Of course, the specific values of the errors do change from one xc-functional to

another and may change when using different codes, pseudo-potentials, or sets of calculation details.

### 3. Effects on thermodynamic properties

#### 3.1 Reaction energies and equilibrium potentials

A variable of great interest in electrochemistry is the equilibrium potential ( $U^0$ ), which indicates the maximum voltage a spontaneous redox reaction can deliver or, conversely, the minimum voltage that must be supplied to drive a nonspontaneous redox reaction.<sup>59</sup> Moreover, the equilibrium potential is necessary to calculate the thermodynamic overpotential, which is often used by CHE-based models as a metric for the catalytic activity of materials. In this order of ideas, the equilibrium potential is a reference point for the optimization and design of catalysts, both in theory and experiments.<sup>1,60–63</sup>

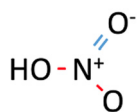
For a reduction reaction,  $U^0$  is related to the reaction Gibbs energy ( $\Delta_r G$ ) and the number of transferred electrons ( $n$ ) by means of eqn (11).



**Table 2** Two matrix representations of nitrogen compounds.<sup>28</sup> The columns under “bonds” represent the molecules in terms of the bonds present in the structure, as used in AO1. The columns under “groups of atoms” decompose the molecules in groups of two or three atoms, as used in AO2. The values show the number of instances each bond and group of atoms are found in the molecules. A negative number is used for *cis*-N<sub>2</sub>O<sub>2</sub> in the groups of atoms to avoid the double counting of its NN group. As NH bonds are usually well described, they are not considered in the analysis. Data taken from ref. 28, licensed under CC BY 4.0 (<https://creativecommons.org/licenses/by/4.0/>)

Species	Bonds				Groups of atoms			
	N–O	N=O	N–N	O–H	ONO	NNO	NOH	NN
NH <sub>2</sub> OH	1	0	0	1	0.0	0.0	1.0	0.0
NO	0	1	0	0	0.0	0.0	0.0	0.0
HNO	0	1	0	0	0.0	0.0	0.0	0.0
NO <sub>2</sub>	1	1	0	0	1.0	0.0	0.0	0.0
NO <sub>3</sub>	2	1	0	0	1.5	0.0	0.0	0.0
<i>trans</i> -HNO <sub>2</sub>	1	1	0	1	0.5	0.0	1.0	0.0
<i>cis</i> -HNO <sub>2</sub>	1	1	0	1	0.5	0.0	1.0	0.0
HNO <sub>3</sub>	2	1	0	1	1.0	0.0	1.0	0.0
N <sub>2</sub> O	0	1	1	0	0.0	1.0	0.0	0.0
<i>cis</i> -N <sub>2</sub> O <sub>2</sub>	0	2	1	0	0.0	2.0	0.0	–1.0
N <sub>2</sub> O <sub>3</sub>	1	2	1	0	1.0	1.0	0.0	0.0
N <sub>2</sub> O <sub>4</sub>	2	2	1	0	2.0	0.0	0.0	1.0
N <sub>2</sub> O <sub>5</sub>	4	2	0	0	2.0	0.0	2.0	0.0

(a) AO1 on HNO<sub>3(g)</sub>



(b) AO2 on HNO<sub>3(g)</sub>

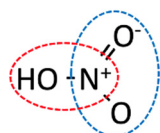


**Fig. 5** (a) Chemical bonds present in HNO<sub>3(g)</sub> as identified in AO1: N–O in red and N=O in blue. (b) NOH (encircled in red) and ONO backbones (enclosed in blue) identified in HNO<sub>3(g)</sub> as per AO2.

$$U^0 = -\Delta_r G/n \quad (11)$$

Eqn (11) shows that if gas-phase errors lead to ill-calculated Gibbs energies, the equilibrium potential will also be affected. For instance, this has been illustrated for the CO<sub>2</sub>RR to CO, where the gas-phase errors lead to a DFT-calculated reaction energy that differs by ~0.4 eV from experiments and the equilibrium potential differs by ~220 mV from the experimental value.<sup>34</sup> It also follows from eqn (11) that the errors in  $U^0$  are typically smaller than for  $\Delta_r G$ , as  $n$  is usually equal to or larger than two in electrocatalytic reactions. As a result, small errors in  $U^0$  may not be indicative of a good description of the gas phase. This has been shown for the electrochemical ammonia synthesis reaction using PBE: its reaction energy deviates by 0.34 eV, whereas its equilibrium potential is only shifted by ~57 mV.<sup>29</sup>

Table 4 compares the DFT-calculated Gibbs energies and equilibrium potentials with experiments for five reactions. The predictions of different xc-functionals are shown in each case. The last column shows that the errors (DFT minus experiments) in the equilibrium potential ( $\epsilon_{U^0}$ ) are a fraction of the

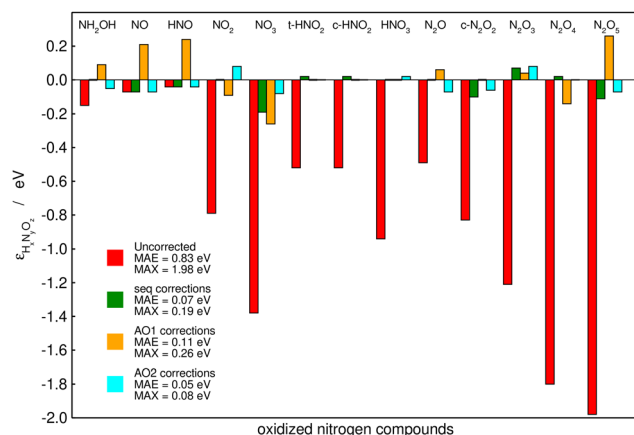


**Fig. 6** Initial and final errors in the PBE-calculated Gibbs energies of thirteen nitrogen compounds after being corrected by a chemically intuitive sequential approach (in green), an automated bond-based approach (AO1, in orange), and an automated version of the chemically intuitive, sequential approach (AO2, in cyan). Reproduced from ref. 28, licensed under CC BY 4.0 (<https://creativecommons.org/licenses/by/4.0/>).

**Table 3** PBE-calculated errors in bonds and groups of atoms present in the nitrogen compounds in Table 2 and Fig. 6, as predicted by three different approaches. Data taken from ref. 28, licensed under CC BY 4.0 (<https://creativecommons.org/licenses/by/4.0/>)

Method	N–H	N–O	N=O	N–N	O–H	NOH	ONO	NNO
AO1	0.00	–0.42	–0.29	–0.26	0.18	—	—	—
AO2	0.00	—	—	–0.07	—	–0.09	–0.87	–0.42
Sequential	0.00	—	—	–0.24	—	–0.15	–0.79	–0.49

errors in the Gibbs energy ( $\epsilon_{\Delta_r G}$ ). In fact, for the CO<sub>2</sub> reduction to CH<sub>4</sub> (last row), the substantial BEEF-vdW free-energy error of 0.81 eV yields an equilibrium potential error of only ~100 mV.

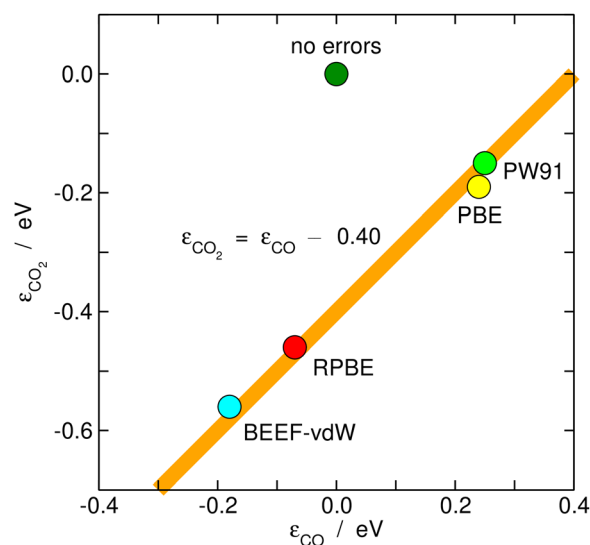


**Fig. 7** Correlation between the gas-phase errors in CO and CO<sub>2</sub> for various xc-correlation functionals. The hypothetical perfect agreement between DFT and experimental values is marked in dark green.





**Table 4** DFT-calculated Gibbs energies and equilibrium potentials using several xc-functionals along with the experimental values (found next to each chemical reaction). In the fourth and fifth columns, the errors in the free energy and equilibrium potential ( $\varepsilon_{\Delta_r G}$  and  $\varepsilon_{U^0}$ , respectively) are shown for each xc-functional. The Gibbs energies are given in eV and the potentials in V vs. RHE

Reaction	xc-Functional <sup>a</sup>	DFT		Error	
		$\Delta_r G$	$U^0$	$\varepsilon_{\Delta_r G}$	$\varepsilon_{U^0}$
(1) $\text{O}_{2(g)} + 2\text{H}^+_{(aq)} + 2\text{e}^- \rightarrow \text{H}_2\text{O}_{2(aq)}$ $\Delta_r G = -1.36$ $U^0 = 0.68$	PBE <sup>64</sup>	-1.14	0.57	0.22	-0.11
	RPBE <sup>64</sup>	-0.90	0.45	0.46	-0.23
	BEEF-vdW <sup>64</sup>	-0.88	0.44	0.48	-0.24
	SCAN <sup>64</sup>	-1.10	0.55	0.26	-0.13
	TPSS <sup>64</sup>	-0.92	0.46	0.44	-0.22
	PBE0 <sup>64</sup>	-1.18	0.59	0.18	-0.09
	B3LYP <sup>64</sup>	-1.12	0.56	0.24	-0.12
(2) $\text{O}_{2(g)} + 4\text{H}^+_{(aq)} + 4\text{e}^- \rightarrow 2\text{H}_2\text{O}_{(l)}$ $\Delta_r G = -4.92$ $U^0 = 1.23$	PBE <sup>26</sup>	-4.46	1.11	0.46	-0.12
	RPBE <sup>26</sup>	-4.18	1.04	0.74	-0.19
	BEEF-vdW <sup>26</sup>	-4.11	1.03	0.81	-0.20
	SCAN	-4.45	1.11	0.47	-0.12
	TPSS	-4.06	1.01	0.86	-0.22
	PBE0	-4.68	1.17	0.24	-0.06
	B3LYP	-4.57	1.14	0.35	-0.09
(3) $\text{N}_{2(g)} + 6\text{H}^+_{(aq)} + 6\text{e}^- \rightarrow 2\text{NH}_{3(g)}$ $\Delta_r G = -0.34$ $U^0 = 0.06$	PBE <sup>29</sup>	-0.68	0.11	-0.34	0.06
	RPBE <sup>29</sup>	-0.31	0.05	0.03	0.00
	BEEF-vdW <sup>29</sup>	-0.03	0.01	0.31	-0.05
	SCAN	-0.67	0.11	-0.33	0.05
	TPSS <sup>29</sup>	-0.19	0.03	0.15	-0.02
	PBE0 <sup>29</sup>	-0.91	0.15	-0.57	0.09
	B3LYP <sup>29</sup>	-0.48	0.08	-0.14	0.02
(4) $\text{CO}_{2(g)} + 8\text{H}^+_{(aq)} + 8\text{e}^- \rightarrow \text{CH}_{4(g)} + 2\text{H}_2\text{O}_{(g)}$ $\Delta_r G = -1.17$ $U^0 = 0.15$	PBE <sup>34</sup>	-0.97	0.12	0.20	-0.03
	RPBE <sup>34</sup>	-0.65	0.08	0.52	-0.07
	BEEF-vdW <sup>34</sup>	-0.36	0.05	0.81	-0.10
	SCAN	-1.08	0.14	0.09	-0.01
	TPSS	-0.59	0.07	0.58	-0.07
	PBE0	-1.37	0.17	-0.20	0.02
	B3LYP	-1.01	0.13	0.16	-0.02
(5) <sup>b</sup> $2\text{NO}_3^-_{(aq)} + 12\text{H}^+_{(aq)} + 10\text{e}^- \rightarrow \text{N}_{2(g)} + 6\text{H}_2\text{O}_{(l)}$ $\Delta_r G = -12.44$ $U^0 = 1.24$	PBE	-10.22	1.02	2.22	-0.22
	RPBE	-10.26	1.03	2.17	-0.22
	BEEF-vdW	-10.10	1.01	2.34	-0.23
	SCAN	-10.95	1.10	1.48	-0.15
	TPSS	-10.08	1.01	2.36	-0.24
	PBE0	-11.51	1.15	0.93	-0.09
	B3LYP	-11.79	1.18	0.64	-0.06

<sup>a</sup> The values for the unreferenced functionals were obtained in this work. <sup>b</sup> Calculations of  $\text{NO}_{3(aq)}^-$  are based on the DFT-energies reported in ref. 29 and experimental data<sup>36</sup> following the approach in ref. 51. In all the cases, the differences between the integral of the specific heats of the products and reactants from 0 K to 298.15 K were neglected when computing the DFT free energies of reaction.

Again, we stress that small errors in equilibrium potentials are not necessarily indicative of agreement between DFT and experiments, and resorting to reaction energies is advisable.

The results in Tables 1 and 4 indicate that some xc-functionals provide outstanding results for certain molecules and reactions while performing poorly in other cases. For instance, RPBE displays the lowest errors in  $\Delta_r G$  of the ammonia synthesis reaction (0.03 eV and an error in  $U^0$  of -0.01 V) but displays errors above 0.45 eV for reactions involving oxygen-containing compounds. Similarly, PBE0 outperforms GGA and meta-GGA functionals in nearly all cases except the ammonia synthesis reaction, where it yields the worst prediction (an error of 0.57 eV). That said, some overall conclusions can be extracted: in general, the MAEs of GGA/meta-GGA functionals are similar for reactions (1)–(4) in Table 4 (0.39/0.35 eV, 0.67/0.67 eV, 0.23/0.24 eV, and 0.51/0.34 eV, respectively) and so are the MAXs (0.48/0.44 eV, 0.81/0.86 eV,

0.33/0.34 eV, and 0.81/0.58 eV). Except for the ammonia synthesis reaction, hybrids perform better than GGA and meta-GGA functionals, producing the lowest MAEs and MAXs for the reactions in Table 4 (reaction 1: MAE = 0.21, MAX = 0.24 eV; reaction 2: MAE = 0.29, MAX = 0.35 eV; reaction 4: MAE = 0.18, MAX = 0.20 eV; reaction 5: MAE = 0.79, MAX = 0.93 eV), with B3LYP generally providing the lowest errors. Nevertheless, all these results show that while some functionals perform better than others, the specific errors are generally not small enough to yield accurate predictions (e.g., MAE/MAX values below 0.10 eV). For instance, the errors of B3LYP for reaction 5 are >0.30 eV in Table 4. We note that once the errors are corrected, the experimental results are mimicked by all functionals. Therefore, in general, gas-phase corrections are advisable regardless of the xc-functional used.

Error analyses can also be extended to reactions where solvated and liquid compounds are involved. For aqueous



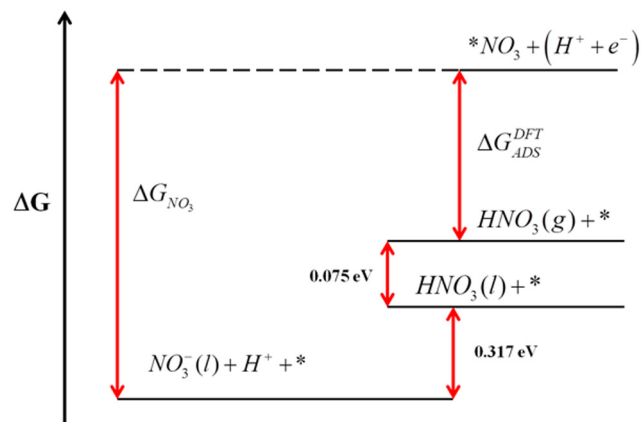


Fig. 8 Gibbs energy scale for  $\text{HNO}_3$  relating the free energies of different states. Reproduced from ref. 51 Copyright 2013, Royal Society of Chemistry.

compounds, the DFT energies of gas-phase references are combined with experimental data to circumvent the DFT modelling of liquids, which is arduous.<sup>1,65–68</sup> A clear example is the DFT modelling of nitrate ( $\text{NO}_3(\text{aq})^-$ ) from gaseous  $\text{HNO}_3$ .<sup>51</sup> In this case, the free energy of gaseous  $\text{HNO}_3$ , easily obtained from DFT, is combined with the experimental vaporization (0.075 eV) and solution free energies (0.317 eV) to indirectly obtain the free energy of  $\text{NO}_3(\text{aq})^-$ ,<sup>36</sup> as shown in Fig. 8. This semiempirical energy can then be used to calculate the equilibrium potential of nitrate reduction reactions. Given that the error in the DFT-calculated free energy of  $\text{HNO}_3$  is larger than 1 eV for several GGA and meta-GGA xc-functionals,<sup>25,28,29,51</sup> overlooking it leads to seriously impaired reaction energies and equilibrium potentials, especially for reactions with small number of transferred electrons.

### 3.2 Adsorption and desorption energies

When modelling electrocatalytic reactions, adsorption and desorption steps occur at least once and are, therefore, central in the analysis. The adsorption of species A on a free surface site (\*) can be represented as follows:



Note that the desorption step is just the opposite process of eqn (12). The Gibbs energy of adsorption can be defined as:

$$\Delta G_{\text{A}}^{\text{ADS}} = G_{* \text{A}} - G_* - G_{\text{A}} \quad (13)$$

As in eqn (1) and (2), an accurate estimation of the adsorption energy of A ( $G_{* \text{A}}$ ) depends on accurate DFT calculations of the total energy of A ( $G_{\text{A}}$ ), usually a gaseous or a liquid/solvated species.<sup>51,66</sup> Thus, gas-phase errors directly affect adsorption/desorption energies.

Besides, gas-phase errors might modify the adsorption/desorption energies such that intermediate adsorption/desorption steps become (or cease to be) limiting in a reaction. In principle, when the binding is considerably modified by gas-phase corrections, opposing strategies to optimize a given catalyst may be obtained before and after the corrections. Consider the coupling reaction  $\text{A}_{(\text{g})} + \text{B}_{(\text{g})} \rightarrow \text{AB}_{(\text{g})}$ , with  $\varepsilon_{\text{AB}}$  representing the DFT gas-phase error of  $\text{AB}_{(\text{g})}$ . Fig. 9 shows the adsorption of A and B, their surface coupling, and the desorption of AB. The inset shows a schematic bar plot for the desorption Gibbs energy of  $\text{AB}_{(\text{g})}$  when the gas-phase errors are not considered and when they are accounted for, the difference being  $\varepsilon_{\text{AB}}$ , following eqn (4). Catalyst deactivation by site blocking is likely to be observed if the magnitude of the correction term  $\varepsilon_{\text{AB}}$  is such that the corrected desorption energy is larger than 0.75 eV, which is an accepted threshold for viable kinetics at room temperature.<sup>69,70</sup> However, this deactivation would not be predicted by the uncorrected results. Further examples are provided in the next sections.

## 4. Implications for free-energy diagrams

### 4.1 Free-energy diagrams

DFT allows us to estimate, within a reasonable timeframe, the energies of adsorbed intermediates, which is something usually not attainable in experiments, in particular for short-lived



Fig. 9 Scheme of a catalytic coupling reaction. Inset: Desorption energy of AB before (in red) and after (in green) correcting gas-phase errors. In the example, without gas-phase errors, easy desorption is predicted, whereas site blocking is predicted upon incorporating them. Adapted from ref. 25 Copyright 2021, John Wiley and Sons.



species. From the Gibbs energies of the intermediates and the CHE model,<sup>1</sup> it is possible to build free-energy diagrams for entire electrochemical reaction networks. These diagrams are used (i) to establish the feasibility of a given reaction pathway at different applied potentials and pH, and (ii) to quantify the catalytic performance of several materials through the identification of the potential-limiting step and the calculation of the overpotential. In fact, free-energy diagrams are arguably the most widespread activity plots in electrocatalysis.<sup>1,6,9,10,71</sup>

**4.1.1 The ideal catalyst.** The free-energy diagram of a reaction on the ideal catalyst allows to determine the best electrocatalytic conversion that complies with the laws of thermodynamics, thus providing a starting point toward the modelling, design and benchmarking of real catalysts.<sup>10,61,72</sup> For the ideal catalyst, all electrochemical steps have the same free energy variation at 0 V vs. RHE, which implies that the reaction energies of those steps are null at the equilibrium potential. In other words, the ideal catalyst is energetically symmetric, and its diagram for a reduction reaction is obtained by dividing the reaction Gibbs energy by the total number of electrochemical steps. Consider the case of oxygen reduction to water: the standard free energy of is  $-4.92$  eV and four electrons are transferred, so at 0 V vs. RHE one has that  $\Delta G_1 = \Delta G_2 = \Delta G_3 = \Delta G_4 = -1.23$  eV.

As mentioned before, if an electrocatalytic reaction involves gas-phase compounds, the DFT errors will affect the equilibrium potentials, which distorts the free-energy diagrams of ideal catalysts. For the 4-electron  $O_2$  reduction and evolution reactions on the ideal catalyst (Table 4),<sup>26</sup> the errors in  $O_2$  ( $\epsilon_{O_2}$ ) are usually above 0.30 eV for several functionals. These errors are not only detrimental to the calculation of the equilibrium potential but also to the energetics of individual reaction steps, preventing the accurate estimation of limiting steps. For instance, the reaction energy for oxygen reduction calculated with RPBE is  $-4.18$  eV, according to Table 4. This means that RPBE predicts that oxygen reduction is not as exothermic as it should (by more than 0.70 eV) and, as a result, the equilibrium potential is as low as 1.04 V vs. RHE. This corresponds to an error of around 200 mV.

Similarly, the oxygen reduction reaction to hydrogen peroxide on the ideal catalyst using several xc-functionals was studied recently (Table 4).<sup>27</sup> This reaction involves the errors in molecular oxygen and hydrogen peroxide,  $\epsilon_{O_2}$  and  $\epsilon_{H_2O_2}$ , which are large and different for GGA, GGA-vdW, meta-GGA, and hybrid xc-functionals.<sup>27</sup> In Fig. 10a, the free-energy diagram for  $H_2O_2$  production at 0 V vs. RHE without gas-phase corrections is shown. Fig. 10b shows the diagram with gas-phase corrections applied only to  $O_2$ . In both cases, the ideal catalyst predicted using experimental data is shown in black. Only when both  $\epsilon_{O_2}$  and  $\epsilon_{H_2O_2}$  are corrected can DFT mimic experiments.

Furthermore, Fig. 10a shows that before  $O_2$  and  $H_2O_2$  are corrected, DFT at different rungs of Jacob's ladder underestimates the reaction energy and the equilibrium potential. As a result, the free-energy diagram of the ideal catalyst deviates considerably from what can be expected from experiments. Once the  $O_2$  error is corrected, DFT gives more negative

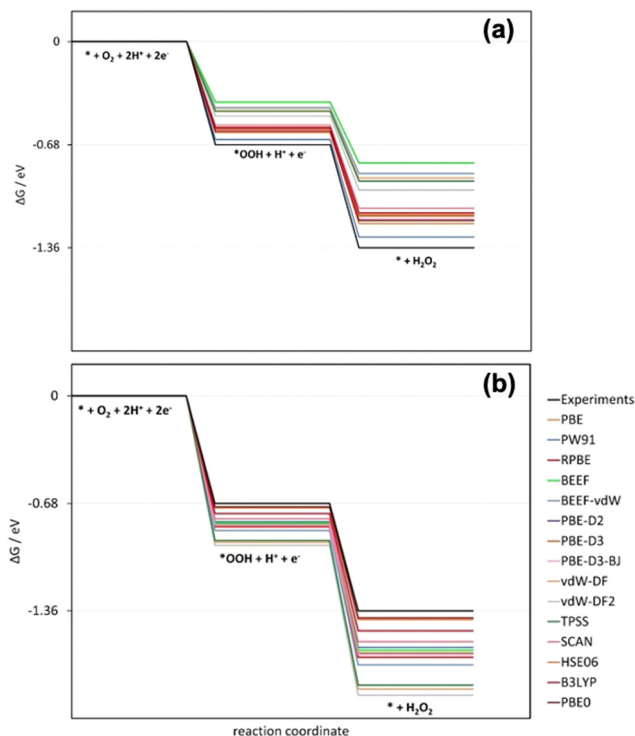


Fig. 10 Free-energy diagrams at 0 V vs. RHE for hydrogen peroxide production on the ideal catalyst using several xc-functionals. (a) Gas-phase corrections are not included. (b) Only the errors in  $O_2$  are corrected. In black in both panels is the experimentally expected profile, obtained when both errors are corrected. Reproduced from ref. 27, licensed under CC BY 4.0 (<https://creativecommons.org/licenses/by/4.0/>).

estimates of all the energies. The switch is introduced by  $\epsilon_{H_2O_2}$ , which is negative for all the DFT functionals scrutinized, see Table 1.

**4.1.2 Real catalysts.** Most often, real catalysts do not display symmetric free-energy diagrams as ideal catalysts do, although enzymes and highly active materials tend to be relatively symmetric.<sup>72–74</sup> This entails additional challenges with respect to the modelling of the ideal catalyst and calls for the concept of onset or limiting potential, which corresponds to the lowest potential guaranteeing that all electrochemical steps along the reaction pathway are downhill in energy (*i.e.*, exergonic). Note that, by definition, the limiting and equilibrium potentials are identical for the ideal catalyst. Within the computational hydrogen electrode model,<sup>1</sup> the effect of the potential ( $U$ ) on the energy of an electrochemical step is given by the term  $eU$  in eqn (14).

$$\Delta_r G(U) = \Delta_r G^\circ + eU \quad (14)$$

where  $\Delta_r G^\circ$  is the reaction energy at SHE conditions (pH = 0,  $T = 298.15$  K, and zero potential).<sup>1</sup>

Limiting potentials may sometimes be affected by gas-phase errors, and free-energy diagrams are suitable tools to visualize and rationalize such effects. In fact, the influence of  $\epsilon_{CO_2}$  and  $\epsilon_{CO}$  has been shown on  $CO_2$  reduction to CO on Au electrodes,<sup>34</sup> and close agreement with experiments is reached if these errors are corrected. Fig. 11 shows the PBE-calculated free-energy



Fig. 11 PBE-calculated free-energy diagrams of the CO<sub>2</sub>RR to CO on Au(111) without (a) and with (b) gas-phase corrections. The Gibbs energies corresponding to the onset and equilibrium potentials are shown in each case along with the experimental onset potential (dashed line). Reproduced from ref. 34, licensed under CC-BY-NC-ND (<https://creativecommons.org/licenses/by-nc-nd/4.0/>).

diagrams of CO<sub>2</sub> reduction to CO following the standard pathway *via* \*COOH and \*CO,<sup>74</sup> with uncorrected and corrected Gibbs energies. For Au(111) electrodes, the first hydrogenation is the potential-limiting step, and the energy decreases from 0.90 to 0.71 eV once the CO<sub>2</sub> Gibbs energy is corrected by −0.19 eV, which is the PBE error for CO<sub>2</sub> (Table 1).<sup>34</sup> Accordingly, the onset potential changes from −0.90 to −0.71 V *vs.* RHE, compared to the experimental onset potential of −0.66 V *vs.* RHE,<sup>75</sup> so the difference with respect to experiments is reduced from 0.24 to 0.05 V once the gas-phase errors are corrected. This analysis was made for numerous metal electrodes and the calculated onset potentials were found to approach the experimental ones upon correcting the DFT errors, see Fig. 12.

We note in passing that free-energy diagrams also show the effects of the gas-phase errors on the reaction energy (and thus on the equilibrium potential), which were previously assessed through eqn (11) in Section 3. In Fig. 11, the reaction energy goes from 0.63 to 0.20 eV, which is the experimental value.<sup>69</sup>

Finally, free-energy diagrams are also affected when intermediate desorption takes place within an electrocatalytic reaction. This can lead to different strategies to optimize a given catalyst, as exemplified in Fig. 13 for the hypothetical electrocatalytic reduction of AB<sub>(g)</sub> to AH<sub>2(g)</sub> and BH<sub>2(g)</sub>, in which four proton-electron transfers take place: AB<sub>(g)</sub> + 4 (H<sup>+</sup> + e<sup>−</sup>) → AH<sub>2(g)</sub> + BH<sub>2(g)</sub>. In this reaction, it is assumed that either (i) AB<sub>(g)</sub> and AH<sub>2(g)</sub> are properly described by DFT ( $\epsilon_{AB} \approx \epsilon_{AH_2} \approx 0$ ) or (ii) have already been corrected, which makes BH<sub>2(g)</sub> the only source of errors. Fig. 13 presents the free-energy diagram of the reaction, considering the energy level of the intermediate desorption of BH<sub>2(g)</sub> with and without gas-phase corrections. Without corrections, the potential-limiting step (PLS<sub>unc</sub>) is the desorption of BH<sub>2(g)</sub> (second proton-electron transfer). After correcting the gas-phase error, the energy of the desorption step decreases by as much as the error in BH<sub>2(g)</sub> ( $\epsilon_{BH_2}$ ) such that the first proton-electron transfer is the actual potential-limiting step (PLS<sub>corr</sub>). The inset

of Fig. 13 depicts how the potential of the second hydrogenation is modified by including the gas-phase correction compared to the energy of the first hydrogenation step. Thence, \*AB → \*ABH should guide the optimization of the catalyst instead of \*ABH → \*A + BH<sub>2(g)</sub>.

## 5. Scaling relations and volcano plots

### 5.1 Scaling relations

When two sets of adsorption energies on various materials are plotted against each other, a linear relationship may emerge, especially when the adsorbates bear some similarities.<sup>76–82</sup> Adsorption-energy scaling relations reveal linear connections between the intermediates of electrocatalytic reactions and enable the making of systematic, trend-based studies to understand the working principle of catalysts and design enhanced active sites.<sup>1,5,11,74</sup> In addition, there are linear relationships between adsorption energies and thermochemical, structural and electronic features of materials, which have been widely used for catalyst screening and design.<sup>83–85</sup> Fig. 14a displays linear relations between the adsorption energies of different atoms (C and Si, N and P, O and S, F and Cl) on top sites of near-surface alloys of Pt(111) and transition metals while Fig. 14b and c show examples of two different sets of adsorption-energy scaling relations: (i) adsorption energies as a function of a structural descriptor, namely the generalized coordination number ( $\overline{CN}$ ),<sup>86–88</sup> and (ii) the adsorption energies of \*OOH, \*O and \*OH as functions of the energies of formation of bulk metal oxides (MO), LaMO<sub>3</sub> perovskites, and SrMO<sub>3</sub> perovskites (M: metals between Ti and Cu).

As discussed in Section 3, DFT gas-phase errors influence adsorption energies. Therefore, gas-phase errors affect adsorption-energy scaling relations. Because the errors are constant for a given xc-functional and a fixed pair of adsorbates, the





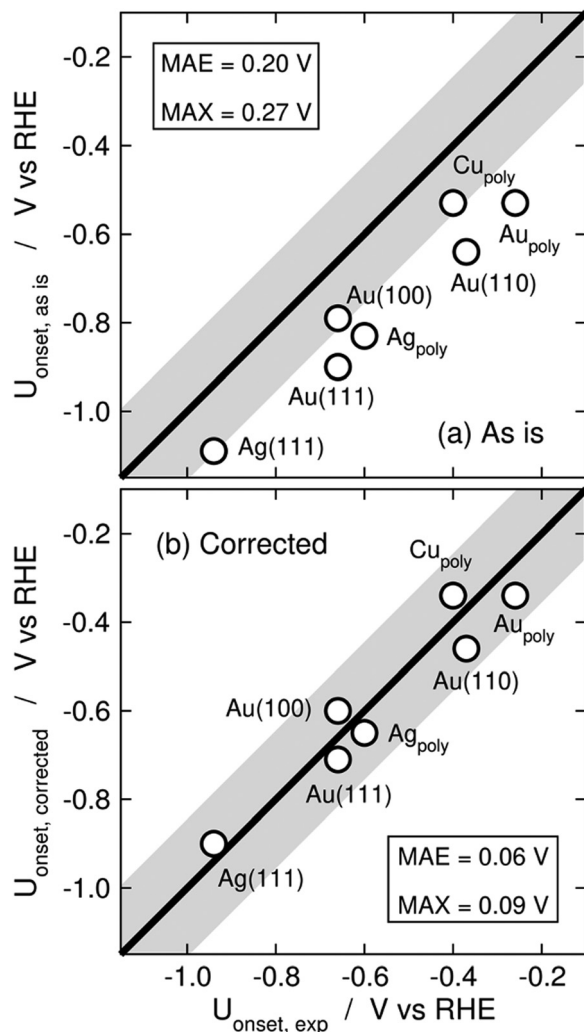


Fig. 12 Parity plots for the PBE-calculated and experimental onset potentials of CO<sub>2</sub> reduction to CO on metal electrodes (a) without and (b) with gas-phase corrections. The MAE and MAX are reported in each case. The gray band around the parity line has a vertical width of 0.2 V. Reproduced from ref. 34, licensed under CC-BY-NC-ND (<https://creativecommons.org/licenses/by-nc-nd/4.0/>).

offsets of scaling relations are modified but the slopes remain unchanged. This is shown in Fig. 15 for the scaling relations between the RPBE-calculated adsorption energies of \*NO<sub>3</sub>, \*NO<sub>2</sub>, and \*NO on a series of metalloporphyrins with different transition-metal centers. Since \*NO<sub>3</sub>, \*NO<sub>2</sub>, and \*NO have sizable gas-phase errors (−1.72, −1.12, and −0.41 eV, respectively), each data point in Fig. 15 is displaced along the direction of the  $\epsilon_T$  vector (in brown) once the energies are corrected. The corresponding abscissa component of  $\epsilon_T$  is the nitric oxide error,  $\epsilon_{NO}$ , whereas the ordinate components correspond to  $\epsilon_{NO_3}$  and  $\epsilon_{NO_2}$  in panels a and b, respectively. For example, in the plot of  $\Delta G_{NO_3}$  vs.  $\Delta G_{NO}$  the uncorrected intercept is 0.47 eV and the slope is 1.76. Given that  $\epsilon_{NO_3} = -1.72$  eV and  $\epsilon_{NO} = -0.41$  eV, the corrected intercept is  $0.47 - 1.72 + 1.76 \times 0.41 = -0.52$  eV.

We note in passing that while scaling relations are conventionally defined for the adsorption energies of two species on

several materials calculated with a fixed computational setup, it is also possible to define them for two species on a given material calculated with various computational setups. Such scaling relations can help detect systematic anomalies in adsorption energies, as illustrated for RuO<sub>2</sub> and \*O, \*OH and \*OOH, for which an anomaly in the adsorption energy of \*O was exposed that explains the incorrect activity prediction for oxygen evolution provided by the CHE for this material.<sup>39,89,90</sup>

## 5.2 Volcano plots

Scaling relations can be used to build Sabatier-type volcano plots, which are extensively used to display the trends in electrocatalytic activity of materials as a function of a given descriptor or a combination of them.<sup>1,11,71,88,91,92</sup> These plots also establish the conditions for optimal catalysis, found at the top of the volcano, and have led to the discovery of promising electrocatalysts for important reactions.<sup>2,76,92,93</sup>

If a metric for the catalytic activity is plotted against the energy of a key intermediate, bidimensional volcanoes are obtained. If the activity is plotted as a function of two or more intermediates, multidimensional volcanoes appear. An example of a bidimensional volcano plot is that of the oxygen evolution reaction on a variety of materials, shown in Fig. 16a. In turn, Fig. 16b is a contour plot relating the binding energies of \*OH and \*C<sub>2</sub>O<sub>2</sub> with the activity for CO electroreduction to ethanol on different metals.

Because scaling relations are modified by gas-phase errors, it is expectable that volcano plots will also be affected by them. The effects depend on whether the limiting steps involve a gas-phase compound, as discussed below. First, let us consider the volcano plot in Fig. 17a for the ASR on metalloporphyrins using the PBE functional and  $\Delta G_{NH_2}$  (\* + NH<sub>3</sub> → \*NH<sub>2</sub> + H<sup>+</sup> + e<sup>−</sup>, with NH<sub>3</sub> assumed to be well-described by DFT,<sup>49</sup> see Section 2, approach iv) as an activity descriptor. In this volcano,  $U_L$  refers to the potential of the limiting reactions and is calculated as  $U_L = -\Delta G_L/n$ , where  $\Delta G_L$  is the energy of the potential-limiting step in eV and  $n$  is the number of electrons transferred (typically 1 for an electrochemical step). Hence, if  $\Delta G_L$  involves gaseous compounds the errors of which are not corrected, it will yield an uncorrected  $U_L$  (red volcano). If the gas-phase errors are taken care of, a corrected  $U_L$  will be obtained (green volcano). The right leg of the volcano is usually limited by the hydrogenation of N<sub>2</sub>, which has a sizable gas-phase error (Table 1), while the left leg is limited by the hydrogenation of adsorbed \*NH<sub>2</sub> to produce NH<sub>3</sub>.<sup>96,97</sup> The reaction on the left leg is not modified by the corrections because NH<sub>3</sub> is thought to be well described by DFT. It is observed in Fig. 17a that upon correcting the errors, the volcano is not symmetrically reshaped, and the impact of that in catalysis is presented in Fig. 18a.

According to recent work,<sup>42</sup> knowledge of the potential-limiting steps suffices to analytically predict the effect of gas-phase errors on volcano plots. This is shown in Fig. 17b for the OER and ORR, which involve the error in O<sub>2</sub>, using four GGA functionals (PBE, PW91, RPBE, and BEEF-vdW).<sup>42</sup> In this figure, the y-axis contains the ORR and OER overpotentials, which are





**Fig. 13** Free-energy diagram of the hypothetical electrocatalytic reduction of  $AB_{(g)}$  to  $AH_{2(g)}$  and  $BH_{2(g)}$ . The Gibbs energies without and with gas-phase corrections for  $BH_2$  are shown in red and green, respectively. PLS: potential-limiting step, which switches from the second ( $PLS_{unc}$ ) to the first hydrogenation step ( $PLS_{corr}$ ) after applying the corrections. Inset: Potential of the second hydrogenation before (red) and after (green) the corrections compared to that of the first hydrogenation (blue).



**Fig. 14** (a) Scaling relations between the adsorption energies of different atoms (C, Si, N, P, O, S, F, Cl) on top sites of near-surface alloys of Pt(111) and transition metals. Reproduced with permission from ref. 78 Copyright 2012, American Physical Society. (b) Adsorption energies of  $*OOH$  and  $*OH$  on different sites at platinum nanoparticles and extended surfaces as a function of the generalized coordination number ( $\overline{CN}$ ). Reproduced with permission from ref. 87 Copyright 2017, AAAS. (c) Correlations between the adsorption energies of  $*OOH$ ,  $*O$ , and  $*OH$  and the formation energy of bulk  $MO$ ,  $LaMO_3$ , and  $SrMO_3$ , where  $M$  is a metal from Ti to Cu. Triangles are data for which the linear relationships do not apply. Reprinted (adapted) with permission from ref. 84 Copyright 2014, American Chemical Society.



Fig. 15 Free energies of adsorption of  $\text{*NO}_3$  (a) and  $\text{*NO}_2$  (b) versus that of  $\text{*NO}$  on metallocporphyrins. Dashed lines and open circles correspond to uncorrected energies, solid lines and solid circles correspond to energies upon gas-phase corrections. Brown vectors on the V-containing porphyrin show the displacements introduced by the respective gas-phase errors. Reproduced from ref. 29, licensed under CC BY 4.0 (<https://creativecommons.org/licenses/by/4.0/>).

defined with respect to the equilibrium potential as  $\eta_{\text{ORR}} = U_{\text{ORR}}^0 - U_{\text{L,ORR}}$  and  $\eta_{\text{OER}} = U_{\text{L,OER}} - U_{\text{OER}}^0$  (and  $U_{\text{ORR}}^0 = U_{\text{OER}}^0$ ). While the use of overpotentials is customary for ORR and OER modelling,  $U_{\text{L}}$  is more used for other reactions. Fig. 17b illustrates one of

the downsides of using overpotentials instead of potentials: overpotentials introduce the gas-phase errors of the overall reaction into the activity.

For the OER, the optimal adsorption energy of  $\text{*OH}$  used as descriptor ( $\Delta G_{\text{OH}}$ , calculated as the free energy of  $\text{*} + \text{H}_2\text{O} \rightarrow \text{*OH} + \text{H}^+ + \text{e}^-$  with water thought to be well described by DFT)<sup>49</sup> does not change across functionals but the lowest overpotential, *i.e.*, the top of the volcano, does change. This stems from the OER being typically limited by reaction steps in which no gas-phase errors are involved ( $\text{*OH} \rightarrow \text{*O} + \text{H}^+ + \text{e}^-$  and  $\text{*O} + \text{H}_2\text{O} \rightarrow \text{*OOH} + \text{H}^+ + \text{e}^-$ ). In striking contrast, both the lowest overpotential and the optimal  $\Delta G_{\text{OH}}$  change depending on the xc-functional for the ORR. This is because one of the potential-limiting steps involves molecular oxygen ( $\text{*} + \text{O}_2 + \text{H}^+ + \text{e}^- \rightarrow \text{*OOH}$ ), which has usually large errors for several functionals. In view of that, the uncorrected ORR volcanoes in Fig. 17b are located to the left and below the corrected volcano. After corrections, the volcanoes of all the xc-functionals turn into the semiempirical one (denoted as SE) as the gas-phase errors are defined with respect to the corresponding experimental values (see eqn (3),  $\varepsilon_{\text{T}} = \Delta_{\text{r}}G_{\text{DFT}} - \Delta_{\text{r}}G_{\text{exp}} = \Delta_{\text{r}}H_{\text{DFT}} - \Delta_{\text{r}}H_{\text{exp}}$ ). Lastly, the equations in Fig. 17b show that the location of the ORR and OER volcano apices can be analytically predicted on the basis of the error in  $\text{O}_2$  for all functionals following simple considerations. Full details can be found in ref. 42.

In principle, the descriptor of a volcano plot may help establish guidelines toward enhanced electrocatalysis. In other words, if the value of the descriptor that corresponds to the top of the volcano is reachable by means of some electronic or structural procedure, rational catalyst design is enabled.<sup>87</sup> Gas-phase errors affect this process, as they mislocate the top of the volcano and alter the activity trends. This is shown for the ASR modelled with PBE in Fig. 18a.<sup>29</sup> Without gas-phase corrections, the strategy to reach the top of the volcano is the opposite as when they are included: the uncorrected volcano



Fig. 16 (a) Volcano plot for oxygen evolution on different materials. Reproduced from ref. 94, licensed under CC-BY 3.0 (<https://creativecommons.org/licenses/by/3.0/>). (b) Contour plot for CO reduction to ethanol on the (100) facet of different transition metals. In both panels, the overpotential is used as a metric for the catalytic activity. Reprinted (adapted) with permission from ref. 95 Copyright 2018, American Chemical Society.

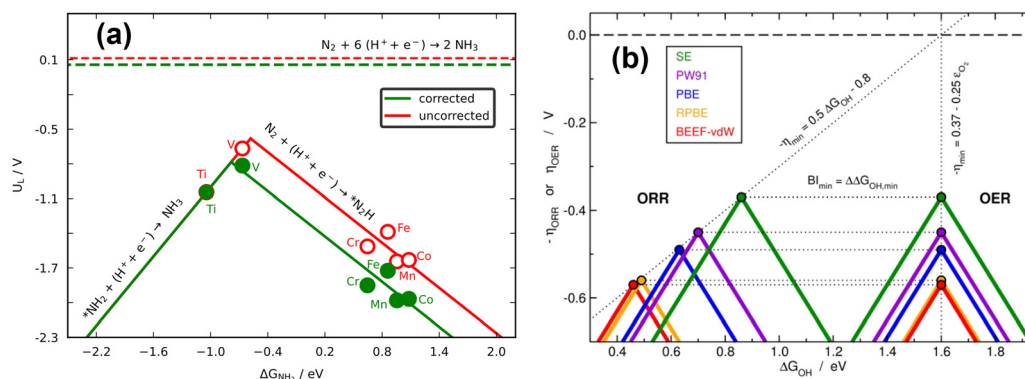


Fig. 17 (a) Volcano plot for electrochemical ammonia synthesis on different metalporphyrins. In red: PBE results with no gas-phase corrections. In green: corrected PBE results. The dashed lines represent the equilibrium potentials. Reproduced from ref. 29, licensed under CC BY 4.0 (<https://creativecommons.org/licenses/by/4.0/>). (b) Volcanoes obtained with four GGAs for the OER and ORR. After accounting for all the gas-phase errors, a single semiempirical volcano (in green, SE) is obtained for each reaction. BI: bifunctional index for the ORR/OER redox performance. Reproduced from ref. 42, licensed under CC BY-NC-ND 4.0 (<https://creativecommons.org/licenses/by-nc-nd/4.0/>).



Fig. 18 (a) Location of V-porphyrin before (in red) and after (in green) correcting the gas-phase errors in electrochemical ammonia synthesis. The arrows show the respective directions towards the top of the volcano. Reproduced from ref. 29, licensed under CC BY 4.0 (<https://creativecommons.org/licenses/by/4.0/>). (b) Effect of compressive/stretching strain and cavities on the catalytic activity of Pt(111) for the ORR with (green) and without (blue) gas-phase corrections. (c) Vertical offsetting of the OER volcano introduced by the error in  $O_2$ . In yellow, an experimental datapoint which is only matched after the gaseous errors are semiempirically corrected. Panels b and c are reproduced from ref. 42, licensed under CC BY-NC-ND 4.0 (<https://creativecommons.org/licenses/by-nc-nd/4.0/>).







Fig. 19 Schematics of gas-phase errors ( $\epsilon_i$ ) and their impact on electrocatalysis models. The origin (brown box), exponential spread (red box), and linear spread (yellow box) in computational (electro)catalysis models are shown. Black steps represent operations performed on different datasets, depicted as blue parallelograms. Data in the blue parallelograms might lead to erroneous quantities if the errors from "Origin" are not corrected.

prescribes the weakening of the adsorption energy of  $\text{*NH}_2$  on the V-porphyrin, whereas the corrected volcano suggests to strengthen it.

Similarly, Fig. 18b illustrates how the PBE errors in  $\text{O}_2$  modify the optimization strategy for the ORR: the uncorrected volcano (in green) displays low activity of cavities and suggests that stretching strain between  $-1\%$  and  $-2\%$  with respect to bulk Pt increases the catalytic activity of pristine Pt(111). Notwithstanding, after correcting the gas-phase errors, compressive strain is predicted to increase the catalytic activity with respect to Pt(111), and small cavities on Pt(111) are closest to the top. In this case, only the corrected volcano plot is in accordance with experiments, which have consistently shown that compressive strain and cavities enhance the activity of Pt(111) electrodes.<sup>87,98–101</sup>

Finally, there are cases in which the symmetric shift of a volcano might take place with concurrent effects on DFT predictions. This is the case for the RPBE-calculated OER volcano on different  $\text{SrRuO}_3$  electrodes (pristine  $\text{SrRuO}_3$ , Na-doped  $\text{SrRuO}_3$ , and  $\text{RuO}_x$  layers on  $\text{SrRuO}_3$ ), as exemplified in Fig. 18c. For this reaction, the potential-limiting steps do not include  $\text{O}_2$ , but the minimum overpotential (the difference between the equilibrium potential and the potential at the top of the volcano) involves  $\epsilon_{\text{O}_2}$ . This means that although the abscissa of the top remains unchanged (at 1.6 eV),  $\epsilon_{\text{O}_2}$  shifts the volcano vertically, leading to larger overpotentials compared to  $\sim 0.37$  V, the value of the corrected model.<sup>10,42,61</sup> Moreover, only after accounting for the gas-phase errors does

the RPBE prediction agree with the experimental datapoint (in yellow) added to the plot on the basis of a semiempirical method.<sup>4,102</sup>

## 6. Summary and outlook

In the previous sections, DFT gas-phase errors were shown to exist at various levels of Jacob's ladder of xc-functionals for numerous molecules. Furthermore, the DFT error ( $\epsilon_i$ ) in the ground-state energy of a gaseous substance or in a set of gaseous compounds (denoted  $E_i^{\text{DFT}}$ ), spreads through customary computational models used in heterogeneous (electro)catalysis, preventing an accurate estimation of paramount quantities such as equilibrium potentials and free energies. In the light of all this, gas-phase errors may mislead the design of active and selective catalysts and/or result in models that only agree with experiments qualitatively, or that agree quantitatively only because of error cancellation.

To summarize all this, Fig. 19 shows the origin, propagation, and spread of gas-phase errors,  $\epsilon_i$ , through computational (electro)catalysis models. The black steps in Fig. 19 represent operations performed on the input datasets, which are depicted in blue. In Fig. 19 we differentiate between linear error spread and exponential error spread: the former is typical of thermodynamic models (yellow box) while the latter is typical of models in which reaction rates are calculated (red box).



A particular example of the spread in the yellow box is found in Fig. 11 and 12, which come from the work of Granda-Marulanda *et al.*<sup>34</sup> together with suitable experimental results<sup>75,103–105</sup> on CO<sub>2(g)</sub> reduction to CO<sub>(g)</sub> on metal electrodes: when modelling this reaction, the uncorrected gas-phase energies lead to a reaction energy of 0.63 eV, which deviates significantly from the experimental value of 0.20 eV (Fig. 11).<sup>69</sup> This wrongful reaction energy yields an equilibrium potential of −0.32 V *vs.* RHE which substantially departs from the experimental value of −0.10 V *vs.* RHE. Moreover, the uncorrected onset potential on Au(111) is 0.90 V *vs.* RHE, which deviates considerably from the experimental value of 0.66 V *vs.* RHE.<sup>75</sup> In striking contrast, if the CO<sub>(g)</sub> and CO<sub>2(g)</sub> energies are corrected, the predicted reaction free energy and equilibrium potential match the experimental values. Furthermore, the corrected energies lead to an onset potential of 0.71 V *vs.* RHE, which differs by only 0.05 V from the experimental value. As shown in Fig. 12, systematic errors are observed for other Au facets and metal electrodes such as Cu and Ag, and the errors disappear upon applying gas-phase corrections.

We hope that the overview provided here encourages the routinary detection and correction of gas-phase errors in computational electrocatalysis studies. That gas-phase errors only shift specific values but leave electrocatalytic activity trends untouched is a common misconception that ought to be rethought. In the following, we provide a list of remaining challenges in this burgeoning area of research.

### 1. Errors in adsorbates

To comprehensively appraise an electrocatalytic reaction, the errors in the adsorbates should be studied in more detail. The energies of adsorbed states are central in the quantification of surface thermochemical properties, and, as the errors in the gas-phase, may have serious implications for electrocatalysis models. Notably, previous works estimated the errors in only a few adsorbates, namely \*COOH, \*OH, \*O, and \*OOH,<sup>39–41</sup> such that further studies are needed. In addition, scaling relations for a given material and using different codes, pseudopotentials and xc-functionals exist. Such scaling relations help assess the accuracy of a given computational electrocatalysis prediction and pinpoint systematic errors in adsorption energies.<sup>39</sup> Exploratory works on this subject would be interesting and insightful.

### 2. Errors in molecular dynamics simulations

If there are errors in static DFT calculations, there should as well be errors in *ab initio* molecular dynamics simulations. Although we are not aware of any work studying those errors, we anticipate that the task is challenging in view of the dynamic nature of the calculations and the large amount of data they comprise.

### 3. Automatization, data availability and transferability

The correction schemes discussed in this work could be automated. Moreover, materials databases, which collect not only experimental data but also results of different *ab initio* calculations,<sup>109</sup> could as well provide information on gas-phase errors. This may bring

further awareness as to the role of gas-phase errors in the predictiveness of high throughput screening routines, big data and machine learning analyses, which are increasingly common in computational chemistry.<sup>110–112</sup> It is worrisome that powerful algorithms are currently learning from uncorrected energy data which, consequently, may lead in many cases to inaccurate predictions. While efforts have been devoted to the assessment of gas-phase errors at different rungs of Jacob's ladder, the transferability of the results from one DFT code to another is yet to be shown. However, the methods for the assessment of the errors presented here are not code dependent.

### 4. New xc-functionals and experimental data

Many xc-functionals are formulated by fitting their parameters to provide, on average, fair estimates of some experimental properties.<sup>52,113</sup> An ideal xc-functional for electrocatalysis is one that simultaneously provides good predictions of reaction energies and adsorption energies, and recent developments point in that direction.<sup>114</sup> Unfortunately, the sets of adsorption energies used to benchmark xc-functionals are currently not large and more experimental data are needed.<sup>21,52,113</sup>

### 5. Uncertainty

Although the choice of descriptor in electrocatalysis is facultative, uncertainty-based analyses can be made that predict the most suitable energetic descriptor for a given reaction.<sup>115</sup> Uncertainty-based analyses have also been used for ORR volcano plots, scaling relations and Pourbaix diagrams.<sup>41,116,117</sup> These analyses could be enriched by fully incorporating gas-phase corrections.

Finally, in addition to adsorption energies and equilibrium potentials, several other factors affect the energetics of electrocatalytic processes and neglecting them may obscure comparisons to experimental results, such as temperature, pressure, electrolyte, pH, mass transport, surface coverage, kinetic and electrochemical potential effects. Improving DFT-based predictions also requires a careful assessment of these factors if one-to-one comparisons to experiments and rationally predictive models are sought after. Recent works are moving along that direction.<sup>7,106–108</sup>

## Conflicts of interest

The authors declare no competing financial interest.

## Acknowledgements

This work received financial support from grants PID2021-127957NB-I00, PID2021-126076NB-I00, TED2021-129506B-C22, TED2021-132550B-C21, and Unidad de Excelencia María de Maeztu CEX2021-001202-M granted to IQTCUB, all funded by MCIN/AEI/10.13039/501100011033 and, in part, by the European Union. The project that gave rise to these results also received the support of a PhD fellowship from “la Caixa” Foundation (ID 100010434, fellowship code LCF/BQ/DI22/11940040). Partial support from COST Action CA18234 and Generalitat de Catalunya 2021SGR00079 grant are also acknowledged.



## References

- 1 J. K. Nørskov, J. Rossmeisl, A. Logadottir, L. Lindqvist, J. R. Kitchin, T. Bligaard and H. Jónsson, Origin of the Overpotential for Oxygen Reduction at a Fuel-Cell Cathode, *J. Phys. Chem. B*, 2004, **108**(46), 17886–17892, DOI: [10.1021/jp047349j](#).
- 2 J. Greeley, T. F. Jaramillo, J. Bonde, I. Chorkendorff and J. K. Nørskov, Computational High-Throughput Screening of Electrocatalytic Materials for Hydrogen Evolution, *Nat. Mater.*, 2006, **5**(11), 909–913, DOI: [10.1038/nmat1752](#).
- 3 Z.-J. Zhao, S. Liu, S. Zha, D. Cheng, F. Studt, G. Henkelman and J. Gong, Theory-Guided Design of Catalytic Materials Using Scaling Relationships and Reactivity Descriptors, *Nat. Rev. Mater.*, 2019, **4**(12), 792–804, DOI: [10.1038/s41578-019-0152-x](#).
- 4 Z. W. Seh, J. Kibsgaard, C. F. Dickens, I. Chorkendorff, J. K. Nørskov and T. F. Jaramillo, Combining Theory and Experiment in Electrocatalysis: Insights into Materials Design, *Science*, 2017, **355**(6321), eaad4998, DOI: [10.1126/science.aad4998](#).
- 5 J. K. Nørskov, T. Bligaard, J. Rossmeisl and C. H. Christensen, Towards the Computational Design of Solid Catalysts, *Nat. Chem.*, 2009, **1**(1), 37–46, DOI: [10.1038/nchem.121](#).
- 6 A. A. Peterson, F. Abild-Pedersen, F. Studt, J. Rossmeisl and J. K. Nørskov, How Copper Catalyzes the Electroreduction of Carbon Dioxide into Hydrocarbon Fuels, *Energy Environ. Sci.*, 2010, **3**(9), 1311, DOI: [10.1039/c0ee00071j](#).
- 7 F. Dattila, R. R. Seemakurthi, Y. Zhou and N. López, Modeling Operando Electrochemical CO<sub>2</sub> Reduction, *Chem. Rev.*, 2022, **122**(12), 11085–11130, DOI: [10.1021/acs.chemrev.1c00690](#).
- 8 X. Zhi, A. Vasileff, Y. Zheng, Y. Jiao and S.-Z. Qiao, Role of Oxygen-Bound Reaction Intermediates in Selective Electrochemical CO<sub>2</sub> Reduction, *Energy Environ. Sci.*, 2021, **14**(7), 3912–3930, DOI: [10.1039/D1EE00740H](#).
- 9 J. K. Nørskov, T. Bligaard, A. Logadottir, J. R. Kitchin, J. G. Chen, S. Pandelov and U. Stimming, Trends in the Exchange Current for Hydrogen Evolution, *J. Electrochem. Soc.*, 2005, **152**(3), J23, DOI: [10.1149/1.1856988](#).
- 10 I. C. Man, H. Su, F. Calle-Vallejo, H. A. Hansen, J. I. Martínez, N. G. Inoglu, J. Kitchin, T. F. Jaramillo, J. K. Nørskov and J. Rossmeisl, Universality in Oxygen Evolution Electrocatalysis on Oxide Surfaces, *ChemCatChem*, 2011, **3**(7), 1159–1165, DOI: [10.1002/cctc.201000397](#).
- 11 A. Kulkarni, S. Siahrostami, A. Patel and J. K. Nørskov, Understanding Catalytic Activity Trends in the Oxygen Reduction Reaction, *Chem. Rev.*, 2018, **118**(5), 2302–2312, DOI: [10.1021/acs.chemrev.7b00488](#).
- 12 C. J. Cramer and D. G. Truhlar, Density Functional Theory for Transition Metals and Transition Metal Chemistry, *Phys. Chem. Chem. Phys.*, 2009, **11**(46), 10757, DOI: [10.1039/b907148b](#).
- 13 M. G. Medvedev, I. S. Bushmarinov, J. Sun, J. P. Perdew and K. A. Lyssenko, Density Functional Theory Is Straying from the Path toward the Exact Functional, *Science*, 2017, **355**(6320), 49–52, DOI: [10.1126/science.aah5975](#).
- 14 J. Paier, M. Marsman and G. Kresse, Why Does the B3LYP Hybrid Functional Fail for Metals?, *J. Chem. Phys.*, 2007, **127**(2), 024103, DOI: [10.1063/1.2747249](#).
- 15 A. Stroppa and G. Kresse, The Shortcomings of Semi-Local and Hybrid Functionals: What We Can Learn from Surface Science Studies, *New J. Phys.*, 2008, **10**(6), 063020, DOI: [10.1088/1367-2630/10/6/063020](#).
- 16 J. Paier, M. Marsman, K. Hummer, G. Kresse, I. C. Gerber and J. G. Ángyán, Screened Hybrid Density Functionals Applied to Solids, *J. Chem. Phys.*, 2006, **124**(15), 154709, DOI: [10.1063/1.2187006](#).
- 17 J. P. Perdew, A. Ruzsinszky, L. A. Constantin, J. Sun and G. I. Csonka, Some Fundamental Issues in Ground-State Density Functional Theory: A Guide for the Perplexed, *J. Chem. Theory Comput.*, 2009, **5**(4), 902–908, DOI: [10.1021/ct800531s](#).
- 18 S. Mallikarjun Sharada, T. Bligaard, A. C. Luntz, G.-J. Kroes and J. K. Nørskov, SBH10: A Benchmark Database of Barrier Heights on Transition Metal Surfaces, *J. Phys. Chem. C*, 2017, **121**(36), 19807–19815, DOI: [10.1021/acs.jpcc.7b05677](#).
- 19 P. Mori-Sánchez, A. J. Cohen and W. Yang, Many-Electron Self-Interaction Error in Approximate Density Functionals, *J. Chem. Phys.*, 2006, **125**(20), 201102, DOI: [10.1063/1.2403848](#).
- 20 A. J. Garza, A. T. Bell and M. Head-Gordon, Nonempirical Meta-Generalized Gradient Approximations for Modeling Chemisorption at Metal Surfaces, *J. Chem. Theory Comput.*, 2018, **14**(6), 3083–3090, DOI: [10.1021/acs.jctc.8b00288](#).
- 21 J. Wellendorff, T. L. Silbaugh, D. Garcia-Pintos, J. K. Nørskov, T. Bligaard, F. Studt and C. T. Campbell, A Benchmark Database for Adsorption Bond Energies to Transition Metal Surfaces and Comparison to Selected DFT Functionals, *Surf. Sci.*, 2015, **640**, 36–44, DOI: [10.1016/j.susc.2015.03.023](#).
- 22 M. Korth and S. Grimme, “Mindless” DFT Benchmarking, *J. Chem. Theory Comput.*, 2009, **5**(4), 993–1003, DOI: [10.1021/ct800511q](#).
- 23 J. Paier, R. Hirschl, M. Marsman and G. Kresse, The Perdew–Burke–Ernzerhof Exchange–Correlation Functional Applied to the G2-1 Test Set Using a Plane-Wave Basis Set, *J. Chem. Phys.*, 2005, **122**(23), 234102, DOI: [10.1063/1.1926272](#).
- 24 C. Adamo, M. Ernzerhof and G. E. Scuseria, The Meta-GGA Functional: Thermochemistry with a Kinetic Energy Density Dependent Exchange–Correlation Functional, *J. Chem. Phys.*, 2000, **112**(6), 2643–2649, DOI: [10.1063/1.480838](#).
- 25 R. Urrego-Ortiz, S. Builes and F. Calle-Vallejo, Fast Correction of Errors in the DFT-Calculated Energies of Gaseous Nitrogen-Containing Species, *ChemCatChem*, 2021, **13**(10), 2508–2516, DOI: [10.1002/cctc.202100125](#).
- 26 E. Sargeant, F. Illas, P. Rodríguez and F. Calle-Vallejo, Importance of the Gas-Phase Error Correction for O<sub>2</sub> When Using DFT to Model the Oxygen Reduction and Evolution Reactions, *J. Electroanal. Chem.*, 2021, **896**, 115178, DOI: [10.1016/j.jelechem.2021.115178](#).
- 27 M. O. Almeida, M. J. Kolb, M. R. V. Lanza, F. Illas and F. Calle-Vallejo, Gas-Phase Errors Affect DFT-Based Electrocatalysis Models of Oxygen Reduction to Hydrogen





- Peroxide, *ChemElectroChem*, 2022, **9**(12), e202200210, DOI: [10.1002/celec.202200210](https://doi.org/10.1002/celec.202200210).
- 28 R. Urrego-Ortiz, S. Builes and F. Calle-Vallejo, Automated *versus* Chemically Intuitive Deconvolution of Density Functional Theory (DFT)-Based Gas-Phase Errors in Nitrogen Compounds, *Ind. Eng. Chem. Res.*, 2022, **61**(36), 13375–13382, DOI: [10.1021/acs.iecr.2c02111](https://doi.org/10.1021/acs.iecr.2c02111).
  - 29 R. Urrego-Ortiz, S. Builes and F. Calle-Vallejo, Impact of Intrinsic Density Functional Theory Errors on the Predictive Power of Nitrogen Cycle Electrocatalysis Models, *ACS Catal.*, 2022, **12**(8), 4784–4791, DOI: [10.1021/acscatal.1c05333](https://doi.org/10.1021/acscatal.1c05333).
  - 30 J. P. Perdew, Jacob's Ladder of Density Functional Approximations for the Exchange–Correlation Energy, *AIP Conference Proceedings*, AIP, Antwerp (Belgium), 2001, vol. 577, pp. 1–20, DOI: [10.1063/1.1390175](https://doi.org/10.1063/1.1390175).
  - 31 F. Calle-Vallejo, J. I. Martínez, J. M. García-Lastra, M. Mogensen and J. Rossmeisl, Trends in Stability of Perovskite Oxides, *Angew. Chem., Int. Ed.*, 2010, **49**(42), 7699–7701, DOI: [10.1002/anie.201002301](https://doi.org/10.1002/anie.201002301).
  - 32 L. Wang, T. Maxisch and G. Ceder, Oxidation Energies of Transition Metal Oxides within the GGA + U Framework, *Phys. Rev. B: Condens. Matter Mater. Phys.*, 2006, **73**(19), 195107, DOI: [10.1103/PhysRevB.73.195107](https://doi.org/10.1103/PhysRevB.73.195107).
  - 33 V. Stevanović, S. Lany, X. Zhang and A. Zunger, Correcting Density Functional Theory for Accurate Predictions of Compound Enthalpies of Formation: Fitted Elemental-Phase Reference Energies, *Phys. Rev. B: Condens. Matter Mater. Phys.*, 2012, **85**(11), 115104, DOI: [10.1103/PhysRevB.85.115104](https://doi.org/10.1103/PhysRevB.85.115104).
  - 34 L. P. Granda-Marulanda, A. Rendón-Calle, S. Builes, F. Illas, M. T. M. Koper and F. Calle-Vallejo, A Semiempirical Method to Detect and Correct DFT-Based Gas-Phase Errors and Its Application in Electrocatalysis, *ACS Catal.*, 2020, **10**(12), 6900–6907, DOI: [10.1021/acscatal.0c01075](https://doi.org/10.1021/acscatal.0c01075).
  - 35 C. J. Bartel, A. W. Weimer, S. Lany, C. B. Musgrave and A. M. Holder, The Role of Decomposition Reactions in Assessing First-Principles Predictions of Solid Stability, *npj Comput. Mater.*, 2019, **5**(1), 4, DOI: [10.1038/s41524-018-0143-2](https://doi.org/10.1038/s41524-018-0143-2).
  - 36 W. M. Haynes, D. R. Lide and T. J. Bruno, *CRC Handbook of Chemistry and Physics*, CRC Press/Taylor And Francis, Boca Raton, FL, 97th edn, 2016, DOI: [10.1201/9781315380476](https://doi.org/10.1201/9781315380476).
  - 37 H. Wan, A. Bagger and J. Rossmeisl, Improved Electrocatalytic Selectivity and Activity for Ammonia Synthesis on Diporphyrin Catalysts, *J. Phys. Chem. C*, 2022, **126**(39), 16636–16642, DOI: [10.1021/acs.jpcc.2c05646](https://doi.org/10.1021/acs.jpcc.2c05646).
  - 38 Z. Fu, M. Wu, Q. Li, C. Ling and J. Wang, A Simple Descriptor for the Nitrogen Reduction Reaction over Single Atom Catalysts, *Mater. Horiz.*, 2023, **10**(3), 852–858, DOI: [10.1039/D2MH01197B](https://doi.org/10.1039/D2MH01197B).
  - 39 L. G. V. Briquet, M. Sarwar, J. Mugo, G. Jones and F. Calle-Vallejo, A New Type of Scaling Relations to Assess the Accuracy of Computational Predictions of Catalytic Activities Applied to the Oxygen Evolution Reaction, *ChemCatChem*, 2017, **9**(7), 1261–1268, DOI: [10.1002/cctc.201601662](https://doi.org/10.1002/cctc.201601662).
  - 40 R. Christensen, H. A. Hansen and T. Vegge, Identifying Systematic DFT Errors in Catalytic Reactions, *Catal. Sci. Technol.*, 2015, **5**(11), 4946–4949, DOI: [10.1039/C5CY01332A](https://doi.org/10.1039/C5CY01332A).
  - 41 R. Christensen, H. A. Hansen, C. F. Dickens, J. K. Nørskov and T. Vegge, Functional Independent Scaling Relation for ORR/OER Catalysts, *J. Phys. Chem. C*, 2016, **120**(43), 24910–24916, DOI: [10.1021/acs.jpcc.6b09141](https://doi.org/10.1021/acs.jpcc.6b09141).
  - 42 E. Sargeant, F. Illas, P. Rodríguez and F. Calle-Vallejo, On the Shifting Peak of Volcano Plots for Oxygen Reduction and Evolution, *Electrochim. Acta*, 2022, **426**, 140799, DOI: [10.1016/j.electacta.2022.140799](https://doi.org/10.1016/j.electacta.2022.140799).
  - 43 J. P. Perdew, K. Burke and M. Ernzerhof, Generalized Gradient Approximation Made Simple, *Phys. Rev. Lett.*, 1996, **77**(18), 3865–3868, DOI: [10.1103/PhysRevLett.77.3865](https://doi.org/10.1103/PhysRevLett.77.3865).
  - 44 M. Ernzerhof and G. E. Scuseria, Assessment of the Perdew–Burke–Ernzerhof Exchange–Correlation Functional, *J. Chem. Phys.*, 1999, **110**(11), 5029–5036, DOI: [10.1063/1.478401](https://doi.org/10.1063/1.478401).
  - 45 D. C. Patton, D. V. Porezag and M. R. Pederson, Simplified Generalized-Gradient Approximation and Anharmonicity: Benchmark Calculations on Molecules, *Phys. Rev. B: Condens. Matter Mater. Phys.*, 1997, **55**(12), 7454–7459, DOI: [10.1103/PhysRevB.55.7454](https://doi.org/10.1103/PhysRevB.55.7454).
  - 46 R. O. Jones and O. Gunnarsson, The Density Functional Formalism, Its Applications and Prospects, *Rev. Mod. Phys.*, 1989, **61**(3), 689–746, DOI: [10.1103/RevModPhys.61.689](https://doi.org/10.1103/RevModPhys.61.689).
  - 47 A. Kiejna, G. Kresse, J. Rogal, A. De Sarkar, K. Reuter and M. Scheffler, Comparison of the Full-Potential and Frozen-Core Approximation Approaches to Density-Functional Calculations of Surfaces, *Phys. Rev. B: Condens. Matter Mater. Phys.*, 2006, **73**(3), 035404, DOI: [10.1103/PhysRevB.73.035404](https://doi.org/10.1103/PhysRevB.73.035404).
  - 48 S. Grindy, B. Meredig, S. Kirklin, J. E. Saal and C. Wolverton, Approaching Chemical Accuracy with Density Functional Calculations: Diatomic Energy Corrections, *Phys. Rev. B: Condens. Matter Mater. Phys.*, 2013, **87**(7), 075150, DOI: [10.1103/PhysRevB.87.075150](https://doi.org/10.1103/PhysRevB.87.075150).
  - 49 S. Kurth, J. P. Perdew and P. Blaha, Molecular and Solid-State Tests of Density Functional Approximations: LSD, GGAs, and Meta-GGAs, *Int. J. Quantum Chem.*, 1999, **75**(4–5), 889–909. [10.1002/\(SICI\)1097-461X\(1999\)75:4/5<889::AID-QUA54>3.0.CO;2-8](https://doi.org/10.1002/(SICI)1097-461X(1999)75:4/5<889::AID-QUA54>3.0.CO;2-8).
  - 50 Y. Guo, X. Cai, S. Shen, G. Wang and J. Zhang, Computational Prediction and Experimental Evaluation of Nitrate Reduction to Ammonia on Rhodium, *J. Catal.*, 2021, **402**, 1–9, DOI: [10.1016/j.jcat.2021.08.016](https://doi.org/10.1016/j.jcat.2021.08.016).
  - 51 F. Calle-Vallejo, M. Huang, J. B. Henry, M. T. M. Koper and A. S. Bandarenka, Theoretical Design and Experimental Implementation of Ag/Au Electrodes for the Electrochemical Reduction of Nitrate, *Phys. Chem. Chem. Phys.*, 2013, **15**(9), 3196–3202, DOI: [10.1039/C2CP44620K](https://doi.org/10.1039/C2CP44620K).
  - 52 J. Wellendorff, K. T. Lundgaard, A. Møgelhøj, V. Petzold, D. D. Landis, J. K. Nørskov, T. Bligaard and K. W. Jacobsen, Density Functionals for Surface Science: Exchange–Correlation Model Development with Bayesian Error Estimation, *Phys. Rev. B: Condens. Matter Mater. Phys.*, 2012, **85**(23), 235149, DOI: [10.1103/PhysRevB.85.235149](https://doi.org/10.1103/PhysRevB.85.235149).
  - 53 W. Wang, S. Dai, X. Li, J. Yang, D. J. Srolovitz and Q. Zheng, Measurement of the Cleavage Energy of Graphite, *Nat. Commun.*, 2015, **6**(1), 7853, DOI: [10.1038/ncomms8853](https://doi.org/10.1038/ncomms8853).





- 54 L. A. Girifalco and R. A. Lad, Energy of Cohesion, Compressibility, and the Potential Energy Functions of the Graphite System, *J. Chem. Phys.*, 1956, **25**(4), 693–697, DOI: [10.1063/1.1743030](#).
- 55 R. Zacharia, H. Ulbricht and T. Hertel, Interlayer Cohesive Energy of Graphite from Thermal Desorption of Polyaromatic Hydrocarbons, *Phys. Rev. B: Condens. Matter Mater. Phys.*, 2004, **69**(15), 155406, DOI: [10.1103/PhysRevB.69.155406](#).
- 56 L. X. Benedict, N. G. Chopra, M. L. Cohen, A. Zettl, S. G. Louie and V. H. Crespi, Microscopic Determination of the Interlayer Binding Energy in Graphite, *Chem. Phys. Lett.*, 1998, **286**(5–6), 490–496, DOI: [10.1016/S0009-2614\(97\)01466-8](#).
- 57 M. Xia, C. Liang, Z. Cheng, R. Hu and S. Liu, The Adhesion Energy Measured by a Stress Accumulation-Peeling Mechanism in the Exfoliation of Graphite, *Phys. Chem. Chem. Phys.*, 2019, **21**(3), 1217–1223, DOI: [10.1039/C8CP06608F](#).
- 58 Z. Liu, J. Z. Liu, Y. Cheng, Z. Li, L. Wang and Q. Zheng, Interlayer Binding Energy of Graphite: A Mesoscopic Determination from Deformation, *Phys. Rev. B: Condens. Matter Mater. Phys.*, 2012, **85**(20), 205418, DOI: [10.1103/PhysRevB.85.205418](#).
- 59 J. C. Kotz, P. Treichel, J. R. Townsend and D. A. Treichel, *Chemistry & Chemical Reactivity*, Cengage Learning, Boston, MA, 10th edn, 2019.
- 60 A. B. Anderson, Volcano Plots and Effective Reversible Potentials for Oxygen Electoreduction, *Electrocatalysis*, 2012, **3**(3–4), 176–182, DOI: [10.1007/s12678-012-0088-z](#).
- 61 M. T. M. Koper, Thermodynamic Theory of Multi-Electron Transfer Reactions: Implications for Electrocatalysis, *J. Electroanal. Chem.*, 2011, **660**(2), 254–260, DOI: [10.1016/j.jelechem.2010.10.004](#).
- 62 K. S. Exner, A Universal Descriptor for the Screening of Electrode Materials for Multiple-Electron Processes: Beyond the Thermodynamic Overpotential, *ACS Catal.*, 2020, **10**(21), 12607–12617, DOI: [10.1021/acscatal.0c03865](#).
- 63 A. M. Appel and M. L. Helm, Determining the Overpotential for a Molecular Electrocatalyst, *ACS Catal.*, 2014, **4**(2), 630–633, DOI: [10.1021/cs401013v](#).
- 64 M. O. Almeida, M. J. Kolb, M. R. V. Lanza, F. Illas and F. Calle-Vallejo, Gas-Phase Errors Affect DFT-Based Electrocatalysis Models of Oxygen Reduction to Hydrogen Peroxide, *ChemElectroChem*, 2022, **9**(12), e20220021, DOI: [10.1002/celec.202200210](#).
- 65 M. Saleheen and A. Heyden, Liquid-Phase Modeling in Heterogeneous Catalysis, *ACS Catal.*, 2018, **8**(3), 2188–2194, DOI: [10.1021/acscatal.7b04367](#).
- 66 F. Calle-Vallejo and M. T. M. Koper, Theoretical Considerations on the Electoreduction of CO to C<sub>2</sub> Species on Cu(100) Electrodes, *Angew. Chem., Int. Ed.*, 2013, **52**(28), 7282–7285, DOI: [10.1002/anie.201301470](#).
- 67 H. H. Heenen, J. A. Gauthier, H. H. Kristoffersen, T. Ludwig and K. Chan, Solvation at Metal/Water Interfaces: An *Ab Initio* Molecular Dynamics Benchmark of Common Computational Approaches, *J. Chem. Phys.*, 2020, **152**(14), 144703, DOI: [10.1063/1.5144912](#).
- 68 X. Zhang, R. S. DeFever, S. Sarupria and R. B. Getman, Free Energies of Catalytic Species Adsorbed to Pt(111) Surfaces under Liquid Solvent Calculated Using Classical and Quantum Approaches, *J. Chem. Inf. Model.*, 2019, **59**(5), 2190–2198, DOI: [10.1021/acs.jcim.9b00089](#).
- 69 S. Nitopi, E. Bertheussen, S. B. Scott, X. Liu, A. K. Engstfeld, S. Horch, B. Seger, I. E. L. Stephens, K. Chan, C. Hahn, J. K. Nørskov, T. F. Jaramillo and I. Chorkendorff, Progress and Perspectives of Electrochemical CO<sub>2</sub> Reduction on Copper in Aqueous Electrolyte, *Chem. Rev.*, 2019, **119**(12), 7610–7672, DOI: [10.1021/acs.chemrev.8b00705](#).
- 70 J. K. Nørskov, F. Studt, F. Abild-Pedersen and T. Bligaard, *Fundamental Concepts in Heterogeneous Catalysis*, John Wiley & Sons, Inc., Hoboken, NJ, USA, 2014, DOI: [10.1002/9781118892114](#).
- 71 A. Rendón-Calle, S. Builes and F. Calle-Vallejo, A Brief Review of the Computational Modeling of CO<sub>2</sub> Electoreduction on Cu Electrodes, *Curr. Opin. Electrochem.*, 2018, **9**, 158–165, DOI: [10.1016/j.coelec.2018.03.012](#).
- 72 C. H. Kjaergaard, J. Rossmeisl and J. K. Nørskov, Enzymatic versus Inorganic Oxygen Reduction Catalysts: Comparison of the Energy Levels in a Free-Energy Scheme, *Inorg. Chem.*, 2010, **49**(8), 3567–3572, DOI: [10.1021/ic900798q](#).
- 73 B. Hinnemann, P. G. Moses, J. Bonde, K. P. Jørgensen, J. H. Nielsen, S. Horch, I. Chorkendorff and J. K. Nørskov, Biomimetic Hydrogen Evolution: MoS<sub>2</sub> Nanoparticles as Catalyst for Hydrogen Evolution, *J. Am. Chem. Soc.*, 2005, **127**(15), 5308–5309, DOI: [10.1021/ja0504690](#).
- 74 H. A. Hansen, J. B. Varley, A. A. Peterson and J. K. Nørskov, Understanding Trends in the Electrocatalytic Activity of Metals and Enzymes for CO<sub>2</sub> Reduction to CO, *J. Phys. Chem. Lett.*, 2013, **4**(3), 388–392, DOI: [10.1021/jz3021155](#).
- 75 N. Todoroki, H. Tei, H. Tsurumaki, T. Miyakawa, T. Inoue and T. Wadayama, Surface Atomic Arrangement Dependence of Electrochemical CO<sub>2</sub> Reduction on Gold: Online Electrochemical Mass Spectrometric Study on Low-Index Au(*hkl*) Surfaces, *ACS Catal.*, 2019, **9**(2), 1383–1388, DOI: [10.1021/acscatal.8b04852](#).
- 76 F. Calle-Vallejo and M. T. M. Koper, First-Principles Computational Electrochemistry: Achievements and Challenges, *Electrochim. Acta*, 2012, **84**, 3–11, DOI: [10.1016/j.electacta.2012.04.062](#).
- 77 S. Vijay, G. Kastlunger, K. Chan and J. K. Nørskov, Limits to Scaling Relations between Adsorption Energies?, *J. Chem. Phys.*, 2022, **156**(23), 231102, DOI: [10.1063/5.0096625](#).
- 78 F. Calle-Vallejo, J. I. Martínez, J. M. García-Lastra, J. Rossmeisl and M. T. M. Koper, Physical and Chemical Nature of the Scaling Relations between Adsorption Energies of Atoms on Metal Surfaces, *Phys. Rev. Lett.*, 2012, **108**(11), 116103, DOI: [10.1103/PhysRevLett.108.116103](#).
- 79 F. Abild-Pedersen, J. Greeley, F. Studt, J. Rossmeisl, T. R. Munter, P. G. Moses, E. Skúlason, T. Bligaard and J. K. Nørskov, Scaling Properties of Adsorption Energies for Hydrogen-Containing Molecules on Transition-Metal Surfaces, *Phys. Rev. Lett.*, 2007, **99**(1), 016105, DOI: [10.1103/PhysRevLett.99.016105](#).



- 80 J. K. Nørskov, F. Abild-Pedersen, F. Studt and T. Bligaard, Density Functional Theory in Surface Chemistry and Catalysis, *Proc. Natl. Acad. Sci. U. S. A.*, 2011, **108**(3), 937–943, DOI: [10.1073/pnas.1006652108](#).
- 81 F. Calle-Vallejo, D. Loffreda, M. T. M. Koper and P. Sautet, Introducing Structural Sensitivity into Adsorption–Energy Scaling Relations by Means of Coordination Numbers, *Nat. Chem.*, 2015, **7**(5), 403–410, DOI: [10.1038/nchem.2226](#).
- 82 A. Brito-Ravicini and F. Calle-Vallejo, Interplaying Coordination and Ligand Effects to Break or Make Adsorption–energy Scaling Relations, *Exploration*, 2022, **2**(2), 20210062, DOI: [10.1002/EXP.20210062](#).
- 83 H.-Y. Su, K. Sun, W.-Q. Wang, Z. Zeng, F. Calle-Vallejo and W.-X. Li, Establishing and Understanding Adsorption–Energy Scaling Relations with Negative Slopes, *J. Phys. Chem. Lett.*, 2016, **7**(24), 5302–5306, DOI: [10.1021/acs.jpcclett.6b02430](#).
- 84 F. Calle-Vallejo, O. A. Díaz-Morales, M. J. Kolb and M. T. M. Koper, Why Is Bulk Thermochemistry a Good Descriptor for the Electrocatalytic Activity of Transition Metal Oxides?, *ACS Catal.*, 2015, **5**(2), 869–873, DOI: [10.1021/cs5016657](#).
- 85 R. Jacobs, J. Hwang, Y. Shao-Horn and D. Morgan, Assessing Correlations of Perovskite Catalytic Performance with Electronic Structure Descriptors, *Chem. Mater.*, 2019, **31**(3), 785–797, DOI: [10.1021/acs.chemmater.8b03840](#).
- 86 F. Calle-Vallejo, J. I. Martínez, J. M. García-Lastra, P. Sautet and D. Loffreda, Fast Prediction of Adsorption Properties for Platinum Nanocatalysts with Generalized Coordination Numbers, *Angew. Chem., Int. Ed.*, 2014, **53**(32), 8316–8319, DOI: [10.1002/anie.201402958](#).
- 87 F. Calle-Vallejo, J. Tymoczko, V. Colic, Q. H. Vu, M. D. Pohl, K. Morgenstern, D. Loffreda, P. Sautet, W. Schuhmann and A. S. Bandarenka, Finding Optimal Surface Sites on Heterogeneous Catalysts by Counting Nearest Neighbors, *Science*, 2015, **350**(6257), 185–189, DOI: [10.1126/science.aab3501](#).
- 88 F. Calle-Vallejo, The ABC of Generalized Coordination Numbers and Their Use as a Descriptor in Electrocatalysis, *Adv. Sci.*, 2023, 2207644, DOI: [10.1002/advs.202207644](#).
- 89 Z. Xu, J. Rossmeisl and J. R. Kitchin, A Linear Response DFT+*U* Study of Trends in the Oxygen Evolution Activity of Transition Metal Rutile Dioxides, *J. Phys. Chem. C*, 2015, **119**(9), 4827–4833, DOI: [10.1021/jp511426q](#).
- 90 Z. Xu and J. R. Kitchin, Tuning Oxide Activity through Modification of the Crystal and Electronic Structure: From Strain to Potential Polymorphs, *Phys. Chem. Chem. Phys.*, 2015, **17**(43), 28943–28949, DOI: [10.1039/C5CP04840K](#).
- 91 A. A. Peterson and J. K. Nørskov, Activity Descriptors for CO<sub>2</sub> Electroreduction to Methane on Transition-Metal Catalysts, *J. Phys. Chem. Lett.*, 2012, **3**(2), 251–258, DOI: [10.1021/jz201461p](#).
- 92 A. J. Medford, A. Vojvodic, J. S. Hummelshøj, J. Voss, F. Abild-Pedersen, F. Studt, T. Bligaard, A. Nilsson and J. K. Nørskov, From the Sabatier Principle to a Predictive Theory of Transition-Metal Heterogeneous Catalysis, *J. Catal.*, 2015, **328**, 36–42, DOI: [10.1016/j.jcat.2014.12.033](#).
- 93 J. Greeley, I. E. L. Stephens, A. S. Bondarenko, T. P. Johansson, H. A. Hansen, T. F. Jaramillo, J. Rossmeisl, I. Chorkendorff and J. K. Nørskov, Alloys of Platinum and Early Transition Metals as Oxygen Reduction Electrocatalysts, *Nat. Chem.*, 2009, **1**(7), 552–556, DOI: [10.1038/nchem.367](#).
- 94 E. Romeo, F. Illas and F. Calle-Vallejo, A General but Still Unknown Characteristic of Active Oxygen Evolution Electrocatalysts, *Chem. Sci.*, 2023, **14**(13), 3622–3629, DOI: [10.1039/D2SC06832J](#).
- 95 S. Hanselman, M. T. M. Koper and F. Calle-Vallejo, Computational Comparison of Late Transition Metal (100) Surfaces for the Electrocatalytic Reduction of CO to C<sub>2</sub> Species, *ACS Energy Lett.*, 2018, **3**(5), 1062–1067, DOI: [10.1021/acsenerylett.8b00326](#).
- 96 E. Skúlason, T. Bligaard, S. Gudmundsdóttir, F. Studt, J. Rossmeisl, F. Abild-Pedersen, T. Vegge, H. Jónsson and J. K. Nørskov, A Theoretical Evaluation of Possible Transition Metal Electro-Catalysts for N<sub>2</sub> Reduction, *Phys. Chem. Chem. Phys.*, 2012, **14**(3), 1235–1245, DOI: [10.1039/C1CP22271F](#).
- 97 L. R. Johnson, S. Sridhar, L. Zhang, K. D. Fredrickson, A. S. Raman, J. Jang, C. Leach, A. Padmanabhan, C. C. Price, N. C. Frey, A. Raizada, V. Rajaraman, S. A. Saiprasad, X. Tang and A. Vojvodic, MXene Materials for the Electrochemical Nitrogen Reduction—Functionalized or Not?, *ACS Catal.*, 2020, **10**(1), 253–264, DOI: [10.1021/acscatal.9b01925](#).
- 98 T. J. P. Hersbach, C. Ye, A. C. Garcia and M. T. M. Koper, Tailoring the Electrocatalytic Activity and Selectivity of Pt(111) through Cathodic Corrosion, *ACS Catal.*, 2020, **10**(24), 15104–15113, DOI: [10.1021/acscatal.0c04016](#).
- 99 M. Escudero-Escribano, P. Malacrida, M. H. Hansen, U. G. Vej-Hansen, A. Velazquez-Palenzuela, V. Tripkovic, J. Schiotz, J. Rossmeisl, I. E. L. Stephens and I. Chorkendorff, Tuning the Activity of Pt Alloy Electrocatalysts by Means of the Lanthanide Contraction, *Science*, 2016, **352**(6281), 73–76, DOI: [10.1126/science.aad8892](#).
- 100 R. M. Kluge, E. Psaltis, R. W. Haid, S. Hou, T. O. Schmidt, O. Schneider, B. Garlyyev, F. Calle-Vallejo and A. S. Bandarenka, Revealing the Nature of Active Sites on Pt–Gd and Pt–Pr Alloys during the Oxygen Reduction Reaction, *ACS Appl. Mater. Interfaces*, 2022, **14**(17), 19604–19613, DOI: [10.1021/acsami.2c03604](#).
- 101 L. Dubau, J. Nelayah, S. Moldovan, O. Ersen, P. Bordet, J. Drnec, T. Asset, R. Chattot and F. Maillard, Defects Do Catalysis: CO Monolayer Oxidation and Oxygen Reduction Reaction on Hollow PtNi/C Nanoparticles, *ACS Catal.*, 2016, **6**(7), 4673–4684, DOI: [10.1021/acscatal.6b01106](#).
- 102 M. Retuerto, L. Pascual, F. Calle-Vallejo, P. Ferrer, D. Gianolio, A. G. Pereira, Á. García, J. Torrero, M. T. Fernández-Díaz, P. Bencok, M. A. Peña, J. L. G. Fierro and S. Rojas, Na-Doped Ruthenium Perovskite Electrocatalysts with Improved Oxygen Evolution Activity and Durability in Acidic Media, *Nat. Commun.*, 2019, **10**(1), 2041, DOI: [10.1038/s41467-019-09791-w](#).



- 103 K. P. Kuhl, T. Hatsukade, E. R. Cave, D. N. Abram, J. Kibsgaard and T. F. Jaramillo, Electrocatalytic Conversion of Carbon Dioxide to Methane and Methanol on Transition Metal Surfaces, *J. Am. Chem. Soc.*, 2014, **136**(40), 14107–14113, DOI: [10.1021/ja505791r](https://doi.org/10.1021/ja505791r).
- 104 N. Hoshi, M. Kato and Y. Hori, Electrochemical Reduction of CO<sub>2</sub> on Single Crystal Electrodes of Silver Ag(111), Ag(100) and Ag(110), *J. Electroanal. Chem.*, 1997, **440**(1–2), 283–286, DOI: [10.1016/S0022-0728\(97\)00447-6](https://doi.org/10.1016/S0022-0728(97)00447-6).
- 105 M. Ma, B. J. Trzeźniewski, J. Xie and W. A. Smith, Selective and Efficient Reduction of Carbon Dioxide to Carbon Monoxide on Oxide-Derived Nanostructured Silver Electrocatalysts, *Angew. Chem., Int. Ed.*, 2016, **55**(33), 9748–9752, DOI: [10.1002/anie.201604654](https://doi.org/10.1002/anie.201604654).
- 106 K. Ojha, K. Doblhoff-Dier and M. T. M. Koper, Double-Layer Structure of the Pt(111)–Aqueous Electrolyte Interface, *Proc. Natl. Acad. Sci. U. S. A.*, 2022, **119**(3), e2116016119, DOI: [10.1073/pnas.2116016119](https://doi.org/10.1073/pnas.2116016119).
- 107 N. Govindarajan, G. Kastlunger, H. H. Heenen and K. Chan, Improving the Intrinsic Activity of Electrocatalysts for Sustainable Energy Conversion: Where Are We and Where Can We Go?, *Chem. Sci.*, 2022, **13**(1), 14–26, DOI: [10.1039/D1SC04775B](https://doi.org/10.1039/D1SC04775B).
- 108 F. You, S. Xi, J. J. Y. Ho, F. Calle-Vallejo and B. S. Yeo, Influence of Copper Sites with Different Coordination on the Adsorption and Electroreduction of CO<sub>2</sub> and CO, *ACS Catal.*, 2023, **13**(16), 11136–11143, DOI: [10.1021/acscatal.3c03197](https://doi.org/10.1021/acscatal.3c03197).
- 109 A. Jain, S. P. Ong, G. Hautier, W. Chen, W. D. Richards, S. Dacek, S. Cholia, D. Gunter, D. Skinner, G. Ceder and K. A. Persson, Commentary: The Materials Project: A Materials Genome Approach to Accelerating Materials Innovation, *APL Mater.*, 2013, **1**(1), 011002, DOI: [10.1063/1.4812323](https://doi.org/10.1063/1.4812323).
- 110 S. Razzaq and K. S. Exner, Materials Screening by the Descriptor  $G_{\max}(\eta)$ : The Free-Energy Span Model in Electrocatalysis, *ACS Catal.*, 2023, **13**(3), 1740–1758, DOI: [10.1021/acscatal.2c03997](https://doi.org/10.1021/acscatal.2c03997).
- 111 Y. Guan, D. Chaffart, G. Liu, Z. Tan, D. Zhang, Y. Wang, J. Li and L. Ricardez-Sandoval, Machine Learning in Solid Heterogeneous Catalysis: Recent Developments, Challenges and Perspectives, *Chem. Eng. Sci.*, 2022, **248**, 117224, DOI: [10.1016/j.ces.2021.117224](https://doi.org/10.1016/j.ces.2021.117224).
- 112 D. Chen, C. Shang and Z.-P. Liu, Machine-Learning Atomic Simulation for Heterogeneous Catalysis, *npj Comput. Mater.*, 2023, **9**(1), 2, DOI: [10.1038/s41524-022-00959-5](https://doi.org/10.1038/s41524-022-00959-5).
- 113 B. Hammer, L. B. Hansen and J. K. Nørskov, Improved Adsorption Energetics within Density-Functional Theory Using Revised Perdew-Burke-Ernzerhof Functionals, *Phys. Rev. B: Condens. Matter Mater. Phys.*, 1999, **59**(11), 7413–7421, DOI: [10.1103/PhysRevB.59.7413](https://doi.org/10.1103/PhysRevB.59.7413).
- 114 Z. Chen, Z. Liu and X. Xu, Accurate Descriptions of Molecule-Surface Interactions in Electrocatalytic CO<sub>2</sub> Reduction on the Copper Surfaces, *Nat. Commun.*, 2023, **14**(1), 936, DOI: [10.1038/s41467-023-36695-7](https://doi.org/10.1038/s41467-023-36695-7).
- 115 D. Krishnamurthy, V. Sumaria and V. Viswanathan, Maximal Predictability Approach for Identifying the Right Descriptors for Electrocatalytic Reactions, *J. Phys. Chem. Lett.*, 2018, **9**(3), 588–595, DOI: [10.1021/acs.jpclett.7b02895](https://doi.org/10.1021/acs.jpclett.7b02895).
- 116 O. Vinogradova, D. Krishnamurthy, V. Pande and V. Viswanathan, Quantifying Confidence in DFT-Predicted Surface Pourbaix Diagrams of Transition-Metal Electrode–Electrolyte Interfaces, *Langmuir*, 2018, **34**(41), 12259–12269, DOI: [10.1021/acs.langmuir.8b02219](https://doi.org/10.1021/acs.langmuir.8b02219).
- 117 S. Deshpande, J. R. Kitchin and V. Viswanathan, Quantifying Uncertainty in Activity Volcano Relationships for Oxygen Reduction Reaction, *ACS Catal.*, 2016, **6**(8), 5251–5259, DOI: [10.1021/acscatal.6b00509](https://doi.org/10.1021/acscatal.6b00509).

